Materials Characterization 209 (2024) 113695

Contents lists available at ScienceDirect

Materials Characterization

journal homepage: www.elsevier.com/locate/matchar

Second life of recycled graphite for sustainable production of multilayer graphene related materials with multiple potential applications

Lorena Alcaraz [a,*], Carlos Díaz-Guerra [b], Rodolfo Fernández-Martínez [c], M. Belén Gómez-Mancebo [c], Belén Sotillo [b], Irene Llorente [a], Félix A. López [a]

[a] Centro Nacional de Investigaciones Metalúrgicas (CENIM), Consejo Superior de Investigaciones Científicas (CSIC), Avda. Gregorio del Amo 8, Madrid 28040, Spain
[b] Departamento de Física de Materiales, Facultad de Ciencias Físicas, Universidad Complutense de Madrid, Plaza de Ciencias 1, Madrid 28040, Spain
[c] División de Química, Departamento de Tecnología, Centro de Investigaciones Energéticas, Medioambientales y Tecnológicas (CIEMAT), Av. Complutense 40, Madrid 28040, Spain

ARTICLE INFO

Keywords:
lithium-ion batteries
Spent LIBs
Recycled graphites
Sustainable sources
Circular materials
Graphene related materials

ABSTRACT

A sustainable route to obtain graphene oxide (GO) and reduced graphene oxide (rGO) with highly competitive properties through the utilization of graphite recycled from spent vehicle's lithium-ion batteries is described. As compared with previous works, our precursor material is representative of a larger-scale recycling procedure, involves the processing of both cathodic and anodic materials, and concerns a larger number of batteries operated in diverse conditions. The morphology, chemical features, structure, and conductivity of the samples have been thoroughly investigated. Results obtained from complementary characterization techniques reveal the correct formation of GO and rGO samples from the recycled graphites. Electrical measurements show that the conductivity of our GO and rGO samples are very similar or even larger than those reported for samples obtained from high-purity natural graphite. These results indicate that our strategy is able to produce good-quality GOs and rGOs with potential applications in different fields, contributing to the circular economy and the recyclability of discarded wastes.

1. Introduction

Due to the great growth of the electric vehicles market, among others, the demand for lithium-ion batteries (LIBs) has dramatically increased. It is actually estimated that the global LIBs demand - in terms of electric vehicles alone - will reach $221 billion by 2024. This constantly growing demand generates in turn more than 2 million tons of spent LIBs, which will mostly be discarded each year after end-of-life [1]. Nowadays, the recovery of valuable metals such as lithium, nickel, cobalt, manganese, copper, and aluminum from different spent batteries has attracted increasing attention due to their great economic and environmental benefits [2–4]. In this sense, most researchers focus their attention on recovering and recycling several metals present in the cathodes of different kinds of batteries [5,6]. Nevertheless, graphite material used in LIBs is a high-tech product with a high added value, so its recovery is of great interest. Actually, recycling and reuse of graphite from anodic material for different final applications play a significant role in relieving the shortage of graphite natural resources as well as environmental protection [6,7]. Moreover, it is important to keep in mind that natural graphite is considered a critical mineral because of its importance to clean energy transition and global supply concentration [8]. According to the graphene flagship consortium guidelines, non-biological waste recyclability constitutes an important milestone to achieve the challenge of sustainable development of graphene-based materials already at the early stages of their commercial exploitation [9]. In this context, recycling graphite from LiBs pays benefits in terms of recyclability, since it uses a commonly discarded by-product of the metal recovering process from exhausted LiBs whilst allowing a cost-effective production of graphene-based materials. This is in perfect agreement with the second principle of the circular economy, which aims to reintroduce end-of-life products back into the economic cycle.

Carbon-based materials are very interesting due to their stable physicochemical properties, which make them useful for several applications. For example, graphene-based materials have been extensively used in supercapacitors, batteries, and fuel cells [10]. Graphene is a 2-D material of conjugated sp^2 carbon atoms arranged in a honeycomb structure. Its unique atomic structure, high electrical conductivity, high elastic modulus, low thermal expansion coefficient, creep resistance,

* Corresponding author.
E-mail address: alcaraz@cenim.csic.es (L. Alcaraz).

https://doi.org/10.1016/j.matchar.2024.113695
Received 6 September 2023; Received in revised form 26 December 2023; Accepted 22 January 2024
Available online 24 January 2024

and high surface area are considered of interest for several high-performance devices in a wide range of technological fields [11]. Graphene and its related materials are actually being investigated for nano-electronic devices [12,13], highly sensitive sensors [14,15], transparent conductive films [16,17], functional composites [18], energy storage [19], catalysis [20], etc.

Among the different methods to obtain graphene-related materials, the top-down approach - which is based on the fundamental idea of extracting layers of graphene from graphite via chemical exfoliation - is the most convenient in terms of high yield, low cost, versatility and scalability [21]. Chemical exfoliation has a huge potential for the synthesis of graphene-based materials for wider technology and industrial applications. Within this route, large amounts of graphene can be produced at a reasonable cost from graphite oxide [22]. Graphene oxide (GO) can be prepared by oxidation of graphite using concentrated acids and strong oxidants and subsequent exfoliation. GO can be reduced to graphene by eliminating the oxygen-containing groups. Reduced GO (rGO) sheets are generally referred to as chemically modified graphene, chemically transformed graphene, or reduced graphene oxide (rGO).

Some authors have reported the obtaining of graphene-related materials from recycled graphite. However, to the best of our knowledge, these works describe the recovery of graphite from a single spent battery, without providing information regarding the age, use or operating conditions of the sample (i.e., the battery), which poises doubts regarding reproducibility and scalability of the recovering processes. Moreover, the recycled graphite was obtained from cathodic materials from portable batteries (i.e. smartphone and laptop devices). In the present work, graphite used as the precursor material for the obtaining of GO and rGO samples is extracted from the black mass recovered from electric and/or hybrid vehicles, which is composed of both cathodic and anodic materials. This starting material is then much more representative of a large-scale recycling process since it involves a higher number of bigger batteries from different sources (vehicles) and operated in diverse conditions. Our work highlights the utilization of recycled graphite obtained from black masses from spent LIBs as a cost-effective and sustainable route to obtain graphene-based materials with highly competitive properties. A detailed comparison of the synthesis, chemical composition, structure and electrical properties of the obtained graphene oxides and reduced graphene oxides, as well as its potential applications is described. The development of high added value products from spent LIBs contributes to the circular economy and the recyclability of wastes which are traditionally discarded.

2. Experimental

2.1. Characterization techniques

Chemical characterization (% and mg.kg^{-1} concentrations) of all samples involved in this study was performed employing wavelength dispersive X-ray fluorescence (XRF) instrument. These measurements were carried out by using an automated AXIOS Malvern-PANalytical spectrometer with a Rh tube.

Elemental analysis was performed with a LECO TruSpec CHN elemental analyzer to assess the carbon content of the samples, which were heated at least up to 900 °C in the presence of oxygen gas. Mineral and organic compounds were oxidized and/or volatilized to carbon dioxide, which was measured by an infrared detection method.

The morphology of the GO and rGO samples was investigated with a FEI Inspect S scanning electron microscope (SEM). The chemical composition of the samples and the corresponding elemental spatial distribution were assessed by energy dispersive X-ray microanalysis (EDX, Bruker Quantax) in a Hitachi TM300 SEM equipped with a backscattered electron detector (BSE). An accelerating voltage of 15 kV was used for EDX measurements. EDX sampling depth exceeds 2 μm in the experimental conditions used in the present work. Hence the obtained information is quite representative of the bulk composition of the investigated materials.

To evaluate the specific surface area of the samples, the Brunauer-Emmett-Teller (BET) method, via N_2 absorption-desorption measurements, was applied using an ASAP 2020 (Micromeritics) system.

Structural characterization was performed by X-ray diffraction (XRD) using a X'Pert Pro (Malvern-Panalytical) diffractometer with Cu K_α radiation ($\lambda = 1.5406$ Å) and operated at 45 kV and 40 mA in Bragg-Brentano geometry. The diffractograms were acquired in the 10-90° (2θ) range, with 0.016° scanning steps. Phase identification and peak analysis were carried out by using the HighScore Plus 4.8 software (Malvern-Panalytical). The mean interlayer spacing (i.e. d_{002}, nm) was calculated using the Bragg's equation (Eq. (1)):

$$d_{002} = \frac{\lambda}{2 \cdot sin\varnothing} \quad (1)$$

where λ is the X-ray wavelength and Ø is the Bragg angle corresponding to the diffraction maximum.

The graphitization degree (g, %) was determined using Eq. (2), proposed by Maire and Mering [23]:

$$g = \frac{0.3440 - d_{002}}{0.3440 - 0.3354} \cdot 100 \quad (2)$$

where 0.3440 nm is the interlayer spacing of the fully non-graphitized carbon, 0.3354 nm is the interlayer spacing of the ideal graphite crystallite, and d_{002} (nm) is the interlayer spacing calculated from XRD measurements.

X-ray photoelectron spectroscopy (XPS) measurements were carried out with a Fisons MT 500 spectrometer using a non-monochromatic Mg K_α X-ray source (1253.6 eV) operating at 300 W. The analysis chamber was kept with a residual pressure within the 10^{-9} Torr range. XPS measurements were carried out to obtain information about the surface chemistry (chemical bonding, functional groups) of the samples. It is worth to mention that this is essentially a surface characterization technique which actually probes the first 5–10 nm of the sample. High-resolution spectra were recorded at a constant pass energy of 20 eV. XPS spectra were analyzed using CasaXPS software (version 2.3.14). After a Shirley-type background subtraction, curve fitting of the C 1S spectra were performed. For graphitic carbon (C=C), the bandgap is small due to the existence of delocalized π orbitals, similar to metal-like systems. This causes the spectrum of graphitic carbon to present a significant asymmetry that must be reflected in the peak shape. For peak fitting, several functions that allow asymmetry could be used such as asymmetric Lorentzian (LA), finite Lorentzian (LF) and the Doniach-Sunjic (DS), among others. In this work, the LF function (LF (0.6,1.1,350,650,3)) was used, since it contains a parameter that suppresses the peak tail and thus minimizes quantification issues. The peak shape of the C 1 s remaining components can be approximated as a symmetric, mixed Gaussian/Lorentzian line shape [24]. The binding energy scale was calibrated using C 1 s sp^2 peak at 284.5 eV. Fourier transform infrared spectroscopy (FTIR) measurements were performed with a Varian 670 spectrometer in transmittance mode. Spectra were recorded in the (1600–600) cm^{-1} range with a 4 cm^{-1} resolution and using the KBr technique.

Micro-Raman and photoluminescence (PL) measurements were performed in a Horiba Jovin-Ybon LabRAM HR800 system on an Olympus BX 41 confocal microscope at room temperature. The samples were initially excited by a He—Ne laser at 633 nm. However, strong luminescence precluded the obtaining of good quality spectra for GO samples. For this reason, Raman spectra from all the investigated materials were also recorded by using the 325 nm line of a He—Cd laser. The spectral resolution of the system used is ~1.5 cm^{-1} for the 633 nm laser and ~ 2 cm^{-1} for the 325 nm laser. In both cases, power density was carefully adjusted in order to maximize signal to noise ratio while avoiding laser-induced structural and compositional changes, since it is well-known that both GO and rGO are prone to suffer these effects when

inadequate excitation conditions are used in Raman experiments. Spectra in the (800–3400) cm^{-1} range were deconvoluted to a sum of Lorentzian profiles to gain insight into the defect structure of the samples. This multi-peak fitting procedure is considered essential for a correct interpretation of Raman spectra of carbon-based materials [25].

The DC conductivity of the samples was measured on a Keithley 2400 source-meter unit by using the home-made system depicted in Fig. 1, which is similar to that previously used to investigate the electromechanical properties of rGO powders in a previous work [26]. Briefly, powders are placed inside a Teflon insulating cylinder. Bottom and top electrodes are stainless steel pistons with a diameter of 7.9 mm. The Teflon cylinder is fitted in the bottom piston. Then, about 2 mg of powder are introduced in the cylinder. Finally, the top piston is fixed to contact on the GO or rGO powder, so the distance between electrodes remains constant during the measurements. In order to obtain the resistivity, a current is passed through the sample, and the voltage drop is measured with a Keithley 2400 source-meter unit. The resistivity of the two steel electrodes in contact is lower than 3 mΩ, ensuring that the recorded voltage drop is due to the GO or rGO material. *V*oltage values were kept between −3 *V* and 3 V to avoid electric field-induced reduction of the samples [27].

2.2. Obtaining of the samples

2.2.1. Obtaining of recycled graphites from spent Li-ion batteries

In order to obtain the corresponding graphites, 100 g of the black mass from spent LIBs from *v*ehicles was first subjected to acidic leaching. Two different leaching conditions were analyzed for comparison purposes. Precisely, the starting black mass was dispersed in 2 M sulfuric acid (H_2SO_4) with 5% (*v*/v) of H_2O_2, or 1.25 M citric acid (CA, $C_6H_8O_7$) with 1% (v/v) of H_2O_2. After leaching for 2 h at 70 °C, the mixtures were filtered, and the obtained solids (respectively labeled G-1 and G-2) were dried for 24 h at 80 °C.

2.2.2. Synthesis of graphene oxide

Graphene oxide was synthesized according to the Marcano-Tour method [27]. In detail, 3 g of recycled graphite (G1 and G2) were weighed, and a 9:1 mixture of concentrated H_2SO_4 and H_3PO_4 (360:40 mL) was added. This mixture was cooled onto crushed ice and then 18 g of $KMnO_4$ were added in small portions within 30 min in order to avoid becoming explosive. The mixture was then heated to 50 °C using a temperature-controlled water bath and stirred for 18 h, turning out into a paste. Subsequently, the content was cooled to room temperature by adding 400 mL of ultrapure water and crushed ice to the mixture to stop the reaction. Then, 10 mL of 30 wt% H_2O_2 was added in order to reduce residual $KMnO_4$ to soluble $MnSO_4$ in an acidic medium, as described in the following reaction:

$$2\ KMnO_4 + 5\ H_2O_2 + 3\ H_2SO_4 \rightarrow 2\ MnSO_4 + K_2SO_4 + H_2O + 5\ O_2 \quad (3)$$

When 30 wt% H_2O_2 was added, bubbling occurred and a bright yellow colour was observed, indicating a high level of oxidation. The obtained yellow-brown suspension was then cooled down to room temperature, transferred to two 400 mL centrifuge tubes, centrifuged at 8000 rpm for 1 h, and the supernatants removed. The remaining mixture was washed repeatedly, with 250 mL 1 M HCl and ultrapure water until the pH of the supernatant achieved 3.5–4. The final sample was placed in a Petri dish to be deep frozen at −80 °C for 48 h and subsequently dried by lyophilization. Finally, the obtained graphene oxides (GO-1 and GO-2) were ground using a blade mill.

2.2.3. Synthesis of reduced graphene oxide

150 mL of 5 $mg{\cdot}mL^{-1}$ aqueous suspension of both GO-1 and GO-2 were prepared. Then, dispersions were successively sonicated in a low power sonication bath for 1 h and with probe sonication for 3 h, yielding stable and well dispersed graphene oxide (GO) dispersions. After that, the solution was sealed in a 250 mL PTFE-lined autoclave and maintained at 120 °C for 48 h. After cooling down to room temperature, the obtained black suspension was transferred to a beaker, and 15 g of ascorbic acid were added. The mixture was then subjected to magnetic stirring for another 24 h. The content of the beaker was transferred to four 80 mL centrifuge tubes and washed with ultrapure water two times by centrifugation at 10000 rpm for 1 h. The product was placed in a ceramic crucible and vacuum-dried at 60 °C for 24 h. The final rGO-1 and rGO-2 were obtained after a thermal annealing treatment using a heating rate of 5 $°C{\cdot}min^{-1}$ to achieve a final temperature of 600 °C, which is maintained for 24 h in inert atmosphere (Ar).

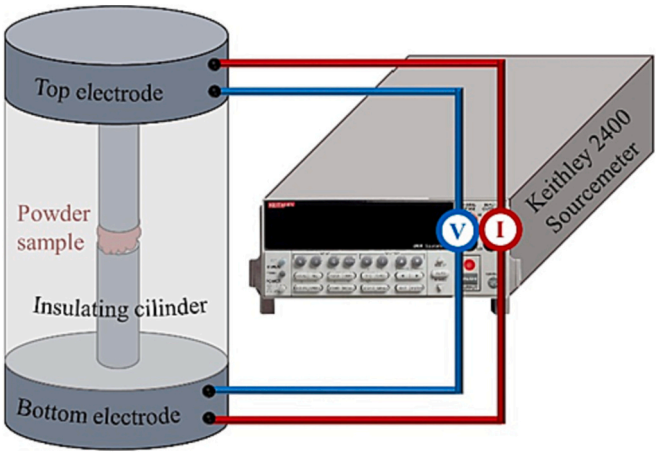

Fig. 1. Experimental setup employed for the electrical characterization of the different GO and rGO powder samples.

3. Results and discussion

The samples synthesized in this work have been extensively characterised in order to gain an in-depth understanding of their properties and thus establish their potential applicability. Precisely, chemical, structural, morphological and electrical characterisations of the samples have been carried out. Samples G1 and G2 have been characterised only by XRF and XRD techniques for their macroscopic evaluation as starting material for the synthesized samples.

3.1. X-ray fluorescence and elemental analysis

Table 1 shows the results obtained from the XRF analysis and EA measurements (C content determination) of the as-prepared samples. All samples show carbon as the most abundant element. Both G1 and G2 samples show a high carbon percentage although this percentage is higher in G1 sample (93%). Due to the more eco-friendly conditions employed in G2, this sample has a slightly higher content of impurities in its composition. Although the starting carbon concentration, in samples G1 and G2, is different, a very similar carbon concentration is obtained in both GO samples (Table 1). As expected, the concentration of carbon in GO samples is around 40%, as oxygenated groups have been introduced between the graphite sheets upon oxidation. These C concentrations are comparable to those measured in GO samples obtained from high-purity (5 N) natural graphite [28]. In the reduced graphene oxide samples, the percentage of C increases again as some of the oxygen content is lost in the form of CO and CO_2. As previously reported in GO samples, the concentrations of carbon obtained in our rGO samples are similar to those obtained when pure graphite was used as starting material [29]. Silicon is also present in both initial samples (G1 and G2). This element remains in all samples (GO and rGO). The origin and this and other impurities will be addressed when discussing SEM-EDX results. In sample G2 there are a few more impurities, due to the more eco-friendly conditions employed. In particular, 1.6% Co and 14% Ni are found. However, the oxidation process applied to the sample is able to

Table 1
Chemical composition (wt% concentration) of graphene-related samples analyzed by XRF and EA (C content).

Sample	G1	G2	GO-1	GO-2	rGO-1	rGO-2
Element	Conc. (%)	Conc. (%)	Conc. (%)	Conc. (%)	Conc. (%)	Conc. (%)
Al	0.26	0.52	0.11	0.12	0.22	0.22
Br	–	–	0.0079	0.0068	–	–
C	93	72	41	40	85	87
Ca	–	0.0036	–	–	0.0072	0.0088
Cl	–	–	0.20	0.17	–	–
Co	0.0022	1.6				
Cr	0.0089	0.0075	–	–	0.0065	0.0079
Cu	0.0072	0.054	–	–	0.0026	0.0015
Fe	0.044	0.024	0.0051	0.0054	0.088	0.14
K	–	–	0.10	0.073	0.017	0.020
Mn	–	–	0.074	0.071	0.061	0.11
Ni	0.018	14	0.0013	0.0064	0.0025	0.011
P	0.041	0.045	0.057	0.053	0.0023	0.0040
Pb	–	–	–	–	0.018	0.019
S	0.017	–	1.5	2.1	0.14	0.14
Si	2.0	2.3	0.55	0.59	1.1	1.3
Ti	0.0026	0.0033	–	–	0.28	0.37
V	–	–	–	–	0.012	0.017
Zn	–	–	–	–	0.0046	0.0037
Zr	0.0016	–	–	–	0.0093	0.31

remove these elements in sample GO-2. In the GO samples, the most abundant element after C was found to be sulfur, which may be partly due to the oxidation process. The concentration of this element strongly decreases in rGO samples as a consequence of thermal annealing.

3.2. Scanning electron microscopy (SEM) and energy dispersive X-ray microanalysis (EDX) microanalysis

The morphology of all the synthesized samples was investigated by scanning electron microscopy (SEM). Fig. 2 shows representative secondary electron images of the GO (a-d) and rGO (e-h) materials. GO samples are made of agglomerates, slightly larger in the case of GO-1, showing a layered wrinkled morphology. The surface of these layers is rather rough and some small particles, with sizes in the (0.5_5) μm range and showing a brighter contrast, can be appreciated in micrographs recorded at higher magnifications. Wrinkled structures are typical of GO prepared by oxidation and mechanical exfoliation of graphite [30]. It is usually related to the compressive stress produced by the surface tension during the drying process [31]. The described morphology is completely different to that observed in rGO materials. For both rGO-1 and rGO-2 samples, the layered structure is somehow lost. Actually, layered structures show a smaller surface and appear well compacted. This fluffy structure typically occurs in rGOs synthesized by thermal reduction due to the stacking of a lot of layers as a consequence of the removal of oxygen-containing functional groups and carbon atoms from the basal plane during thermal treatments [32–34]. In addition, small particles similar to those observed in GO samples can be also observed in the rGO samples.

The chemical composition of the samples, as well as their corresponding elemental spatial distribution, were investigated by energy dispersive X-ray microanalysis (EDX). In all cases, EDX microanalyses (Table 2 and Fig. 3) reveal that carbon and oxygen are the main elements in GO samples, as expected. It should me mentioned that carbon concentrations measured by EA and EDX in rGO samples are quite similar, while a more noticeable difference is found in GO samples. This is probably due to the larger associated error in the determination of light elements contents (C, O) by EDX. In addition, the presence of several impurities in low concentrations is clearly detected. Spectra have been represented in log scale in order to visualize elements present in lower concentrations more clearly. The presence of sulfur, chlorine, manganese, potassium and phosphorous in the GO samples can be attributed to remnants of the chemicals used for the synthesis of this material. The small amount of fluorine detected in sample GO-2 is probably related to rests of the electrolyte in the starting black masses, since electrolyte

Table 2
Quantification of EDX analyses (normalized %wt.) carried out in the GO and rGO samples.

Element	GO-1	GO-2	rGO-1	r-GO2
Carbon	56.25	52.70	88.20	90.30
Oxygen	41.20	42.20	10.00	7.80
Sulfur	1.56	3.21	0.11	0.12
Silicon	0.45	0.61	1.17	1.35
Chlorine	0.17	0.19	–	–
Manganese	0.15	–	–	–
Potassium	0.11	0.10	–	–
Aluminum	0.09	0.17	0.17	0.20
Phosphorous	0.02	0.05	–	–
Fluorine	–	0.77	–	–
Titanium	–	–	0.35	0.23

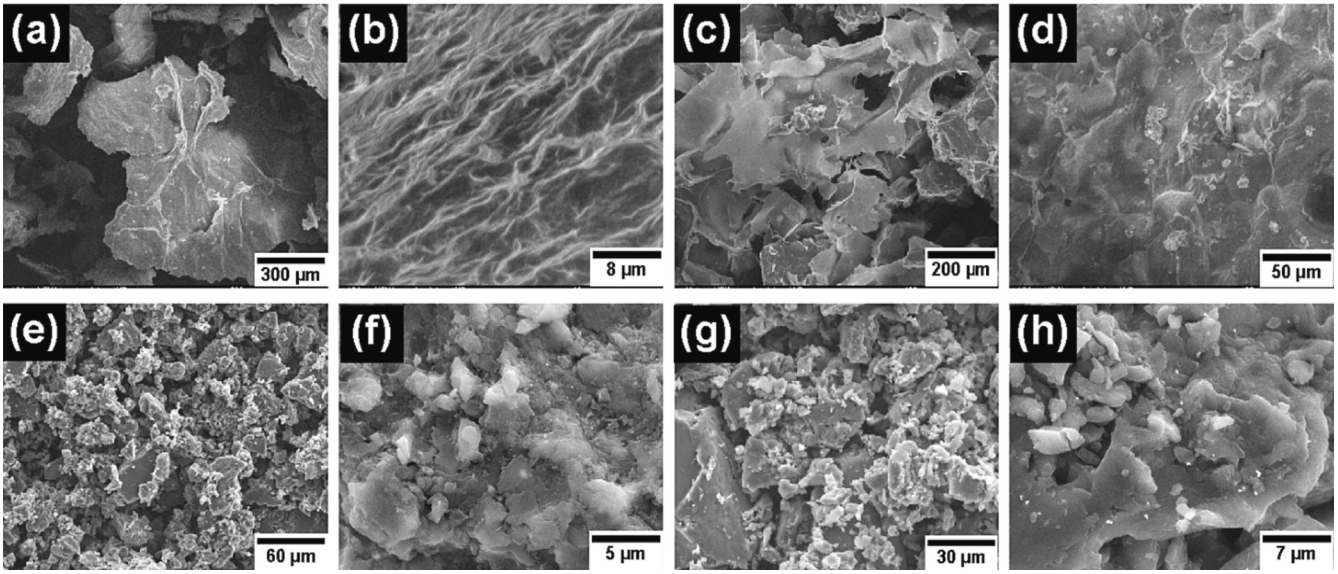

Fig. 2. SEM images of the synthesized samples. (a, b) GO-1, (c, d) GO-2, (e, f) rGO-1, (g, h) rGO-2.

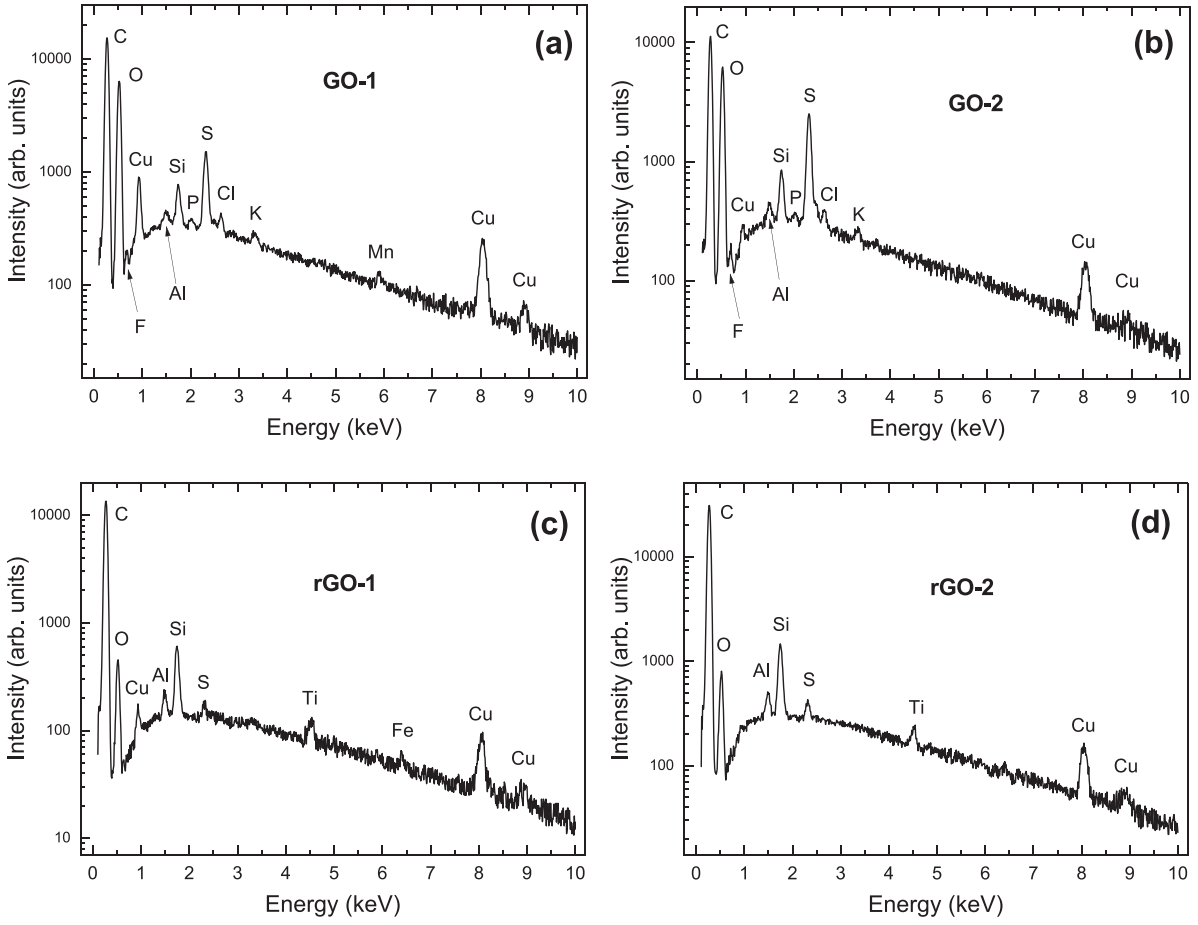

Fig. 3. Representative EDX spectra of the investigated samples. Cu signal stems from the SEM sample holder. Spectra have been represented in log scale in to clearly visualize elements present in low concentrations.

solutions based on fluorinated solvents are frequently employed in LIBs. Silicon and aluminum can be related to the electrical components and the case of the dismantled batteries. These elements are probably present due to the fact that silica and alumina cannot be removed by the H_2SO_4/H_3PO_4 solution used during graphite oxidation or by the HCl solution used during the graphite oxide washing process. The subsequent reduction protocol effectively removes or decreases the concentration of many of these impurities. The presence of titanium in the rGO-samples agrees with the existence of Ti impurities in the precursor graphites. As in the case of Si and Al, this element is hardly removed by the successive washing steps. Moreover, reduction clearly decreases the oxygen content of the GO samples due to the removal of organic groups, increasing the relative carbon concentration measured in rGO samples. The high carbon content measured by EDX suggests a rather strong degree of reduction of the GO samples, similar to rGOs synthesized from natural graphite by combining chemical and thermal reduction [29].

The spatial distribution of the main elements detected in the different samples are shown in Figs. 4–7. Carbon and oxygen distribution are homogeneous throughout the whole material in all the investigated samples. This is also the case for sulfur, chlorine and phosphorous in GO samples. On the contrary, our EDX mappings reveal that Si and Al signals concentrates in small particles showing a bright contrast in BSE images, which is due to the higher atomic number of these elements, as compared with that of carbon. Very often, a clear correlation is observed between Si and O distribution, which strongly suggests the existence of silica particles in both the GO and rGO samples investigated. The absence of the corresponding diffraction maxima in XRD patterns (except G-2), can be explained by the low crystallinity of these particles and/or its small concentration. The correlation is less clear in the case of Al and O spatial distributions, although sometimes is observed as well. As for Ti, which was only detected in rGO samples, signal is found to come from small particles as well unevenly distributed on the C-rich, bigger structures. The spatial distribution of this element is neither correlated with that of Si nor with that of oxygen but sometimes with that of Al (see Fig. 7).

3.3. Brunauer-Emmett-teller (BET) analysis

The Brunauer–Emmett–Teller (BET) method was used to determine the specific surface area. This is an important parameter because it influences the specific capacitance which is directly related to the electrical properties and adsorption capacitance. Specific surface area (SSA) has been calculated only for the final products rGO-1 and rGO-2, since the synthesis of these products causes the greatest expansion of the materials, mainly due to the heat treatment. For both rGO samples, the calculated BET surface areas were of the same order of magnitude with values of 197 m^2/g and 381 m^2/g for rGO-1 and rGO-2, respectively. These remarkable specific surface areas demonstrate that the thermal treatment increases porosity. Although these values are far from the theoretical value of isolated graphene sheets of 2630 $m^2 \cdot g^{-1}$ - which is indicative of grafting due to the agglomeration and partial overlapping of reduced sheets during the thermal reduction process [17]- they are comparable to those reported in rGO samples after similar treatment [35]. It is observed, however, that the SSA obtained for the rGO-2 sample is higher. Taking into account that the procedure applied to G-1 and G-2 recycle graphite samples for the synthesis of GO and rGO is the same, the difference in SSA may be partly due to the acid used in the obtaining of the recycled graphite. In the present case, a higher SSA

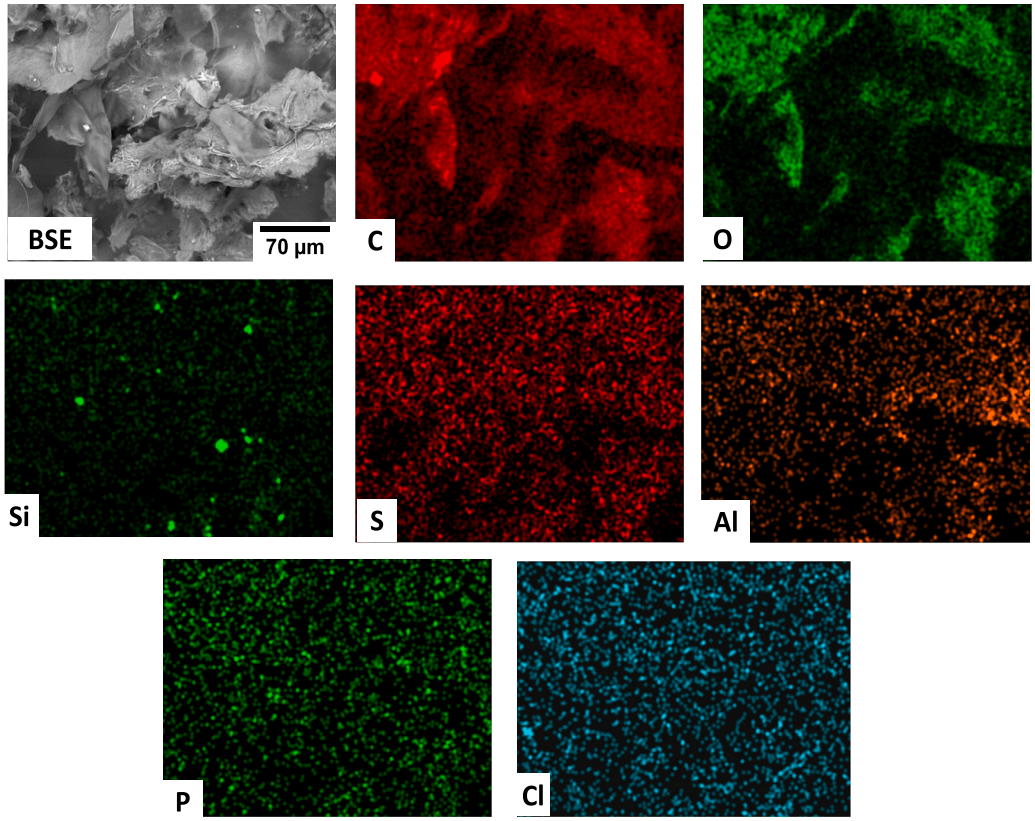

Fig. 4. SEM-EDX mappings from sample GO-1.

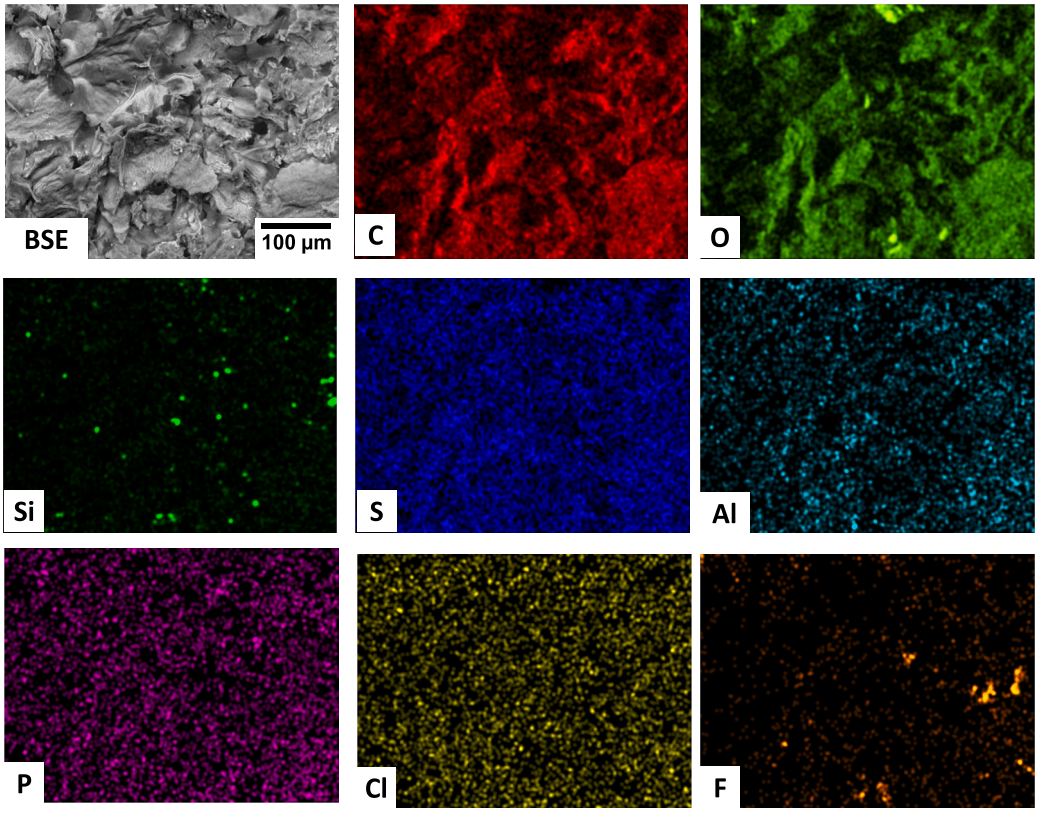

Fig. 5. SEM-EDX mappings from sample GO-2.

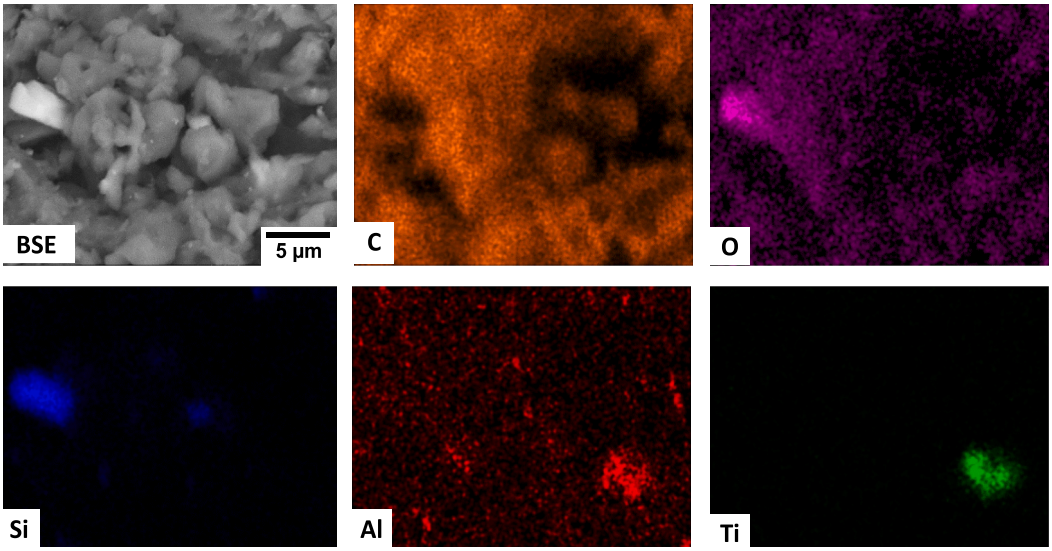

Fig. 6. SEM-EDX mappings from sample rGO-1.

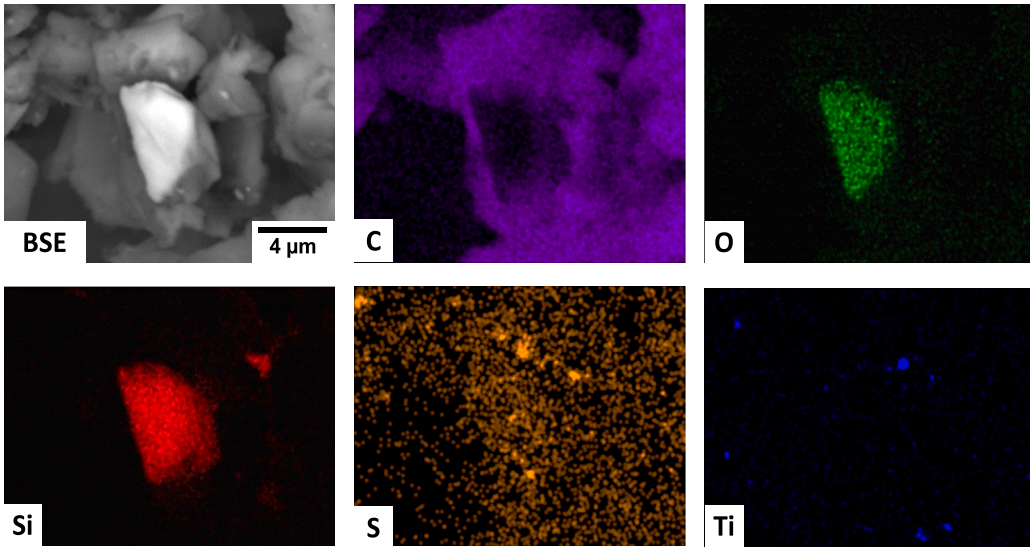

Fig. 7. SEM-EDX mappings from sample rGO-2.

value is obtained with citric acid, which is more ecofriendly. Since rGO-2 is obtained from black mass treated with the mentioned acid, this route offers an attractive compromise between the use of environmentally friendly chemicals and efficient rGO production.

3.4. X-ray diffraction (XRD)

The structural characterization of all obtained samples was first carried out by X-ray diffraction (XRD). Fig. 8 shows representative XRD patterns of the investigated samples. Regarding the recovered graphite samples obtained from spent batteries (i.e. G-1, and G-2), the more intense diffraction maxima can be indexed to the carbon-graphite phase [ICDD 00–041-1487], with hexagonal structure and space group $P6_3/mmc$. The corresponding Miller's indices are also shown in Fig. 8.

The obtained G samples are high-quality graphites as revealed by the calculated mean interlayer spacing (d_{002}) as well as the graphitization degree (g) (Table 3). For both recovered graphite samples, the calculated d_{002} were very similar to that of ideal graphite (0.3354 nm) with d_{002} values of 0.3356 nm and 0.3360 nm for G1 and G2, respectively. In addition, the calculated graphitization degree was 96% for G1 sample, and 91% for G2 sample (Table 3). So, both recovered graphite samples can be classified within graphitic materials [36].

In the particular case of the G2 sample, weaker peaks can also be appreciated. These maxima can be mainly attributed to SiO_2 [96–101-1177], and Al_2O_3 [96–901-6250] as secondary phases. The origin of these impurities is addressed when discussing EDX results. More eco-friendly conditions used in the latest case could lead to graphite with a slightly higher content of impurities in its composition. Actually, another weak diffraction maximum can be attributed to NiO in sample G-2). However, a relatively high Ni concentration is evidenced by XRF in the mentioned sample, which suggests the amorphous nature of the Ni-containing inorganic phase. A similar phenomenon was previously observed in other nanocomposite structures based on graphene-related materials [37]. Fig. 8 also shows XRD patterns of GO and rGO samples. XRD patterns of both GO samples show a dominant diffraction maxima, peaked close to $2\Theta = 11^{o}$ (Table 3), that can be attributed to (001) orientation of GO [38]. In fact, both GO-1 and GO-2 XRD patterns show only two maxima corresponding to graphene oxide. Diffraction maxima associated to impurities present in G1 and G2 are no longer observed. In rGO samples the occurrence of a wide peak at $2\Theta = 23^{o}$

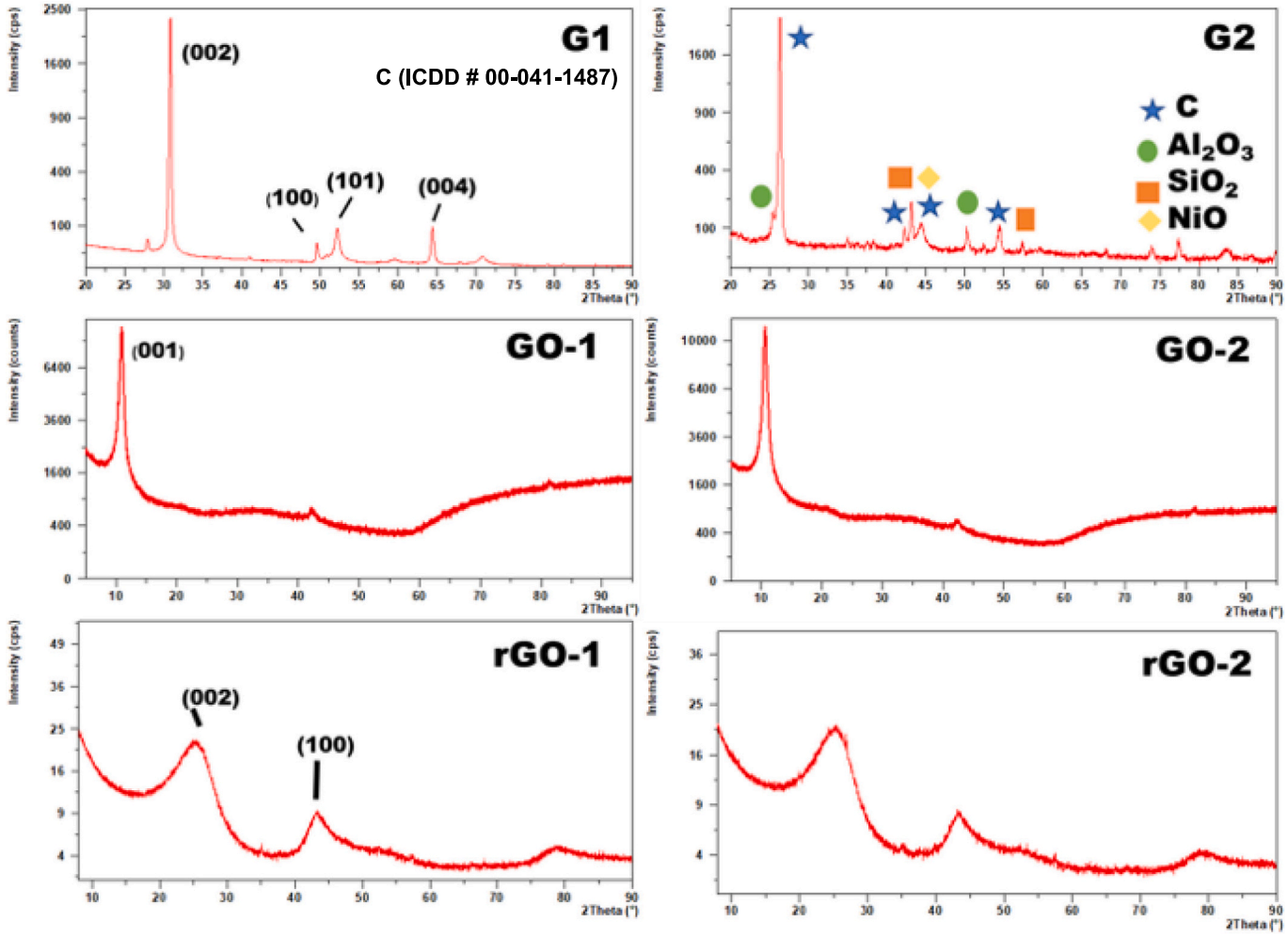

Fig. 8. XRD patterns for recycled graphites from spent lithium-ion batteries, GO and rGO samples.

Table 3
Position of relevant XRD maxima, interlaying spacing and graphitization degree (%) of each sample.

Sample	Position 1 (2 Θ)	Position 2 (2 Θ)	Interlaying spacing (nm)	Graphitization degree (%)
G1	–	26.6637	0.3356	96
G2	–	26.3721	0.3360	91
GO-1	10.835	–	0.8159	–
GO-2	10.5864	–	0.8350	–
rGO-1	–	23.7434	0.3744	–
rGO-2	–	23.2578	0.3815	–

evidences the arrangement of the crystal phase at the orientation (002) [39]. The removal of oxygen-containing functional groups reduces the *d*-spacing of rGO, as compared with GO (Table 3). As in the previous case, the contribution of impurities is not appreciated. Another less intense peak can be observed at $2\Theta \approx 44^{o}$ in rGO samples, which is characteristic of disordered carbon materials, with (100) orientation.

3.5. X-ray photoelectron spectroscopy (XPS)

Fig. 9 shows, as an example, XPS survey spectra of the graphene oxide GO-1 and the reduced graphene oxide rGO-1 samples. The survey scan for the graphene oxide shows the presence of C, O, N, Si, and S. However, reduced graphene oxide sample shows C, O, and Si as constituents. The corresponding quantification of XPS analyses (normalized wt%) of the obtained samples are shown in Table 4.

The C1s spectrum of the samples can be fitted using five individual component peaks (Fig. 10). Generally, the binding energy of the C—C sp^2 and sp^3 bonding are assigned to 284.5 and 285.5 eV, respectively, with a chemical shift distribution of +1.0 eV for the sp^3 bonding; C-O/C-N functional group at 286.0 eV (shifts of 1–1.5 eV to sp^2 binding energy), C═O functional group at 288 eV (shifts from +2.0 to +2.5 eV to sp^2 binding energy) and + 4.0 eV for the COOH functional group (289.3 eV). The relative spectral weights of all these functional groups bands strongly decrease in spectra from rGO samples, as expected after the thermal annealing treatment. Table 5 shows the at.% of the C-containing functional groups as well as the C/O atomic ratio for GO and rGO samples.

According to the analysis of our XPS data, both graphene oxides show very similar Csp^2 percentage and C/O ratio irrespective of the synthesis route followed. In addition, the calculated C/O ratio as well as the different contributions of the organic groups are in close agreement with values calculated for highly hydrophilic GOs obtained from natural graphite after the application of the Tour synthesis method [40]. After reduction, the amount of Csp^2 is very similar in both samples, accounting for 74%, which suggests a significant restoration of sp^2 conjugation comparable with rGOs obtained by high performance reduction treatments [41]. C − O signals decreased more significantly than those from O=C − O, indicating that most of the oxygen functional groups present in GO are removed mainly from the surface rather than edges [42]. In addition, the obtained C/O atomic ratios of 5.80 for rGO1 and 8.09 for rGO2 are notably higher than those found for rGOs obtained

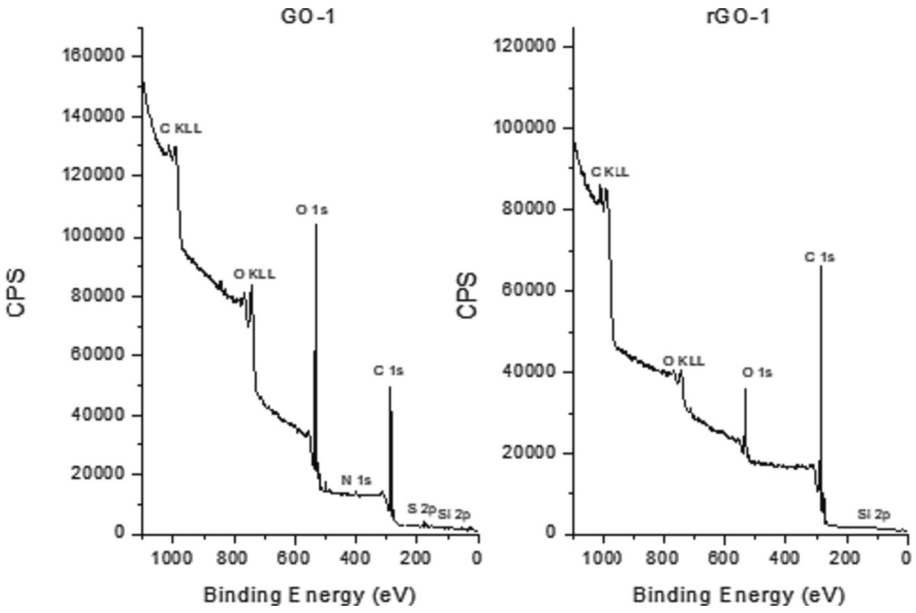

Fig. 9. XPS survey spectra of samples GO-1 and rGO-1.

Table 4
Quantification of XPS analyses (normalized %wt.) carried out in the GO and rGO samples.

Sample	GO-1	GO-2	rGO-1	rGO-2
Carbon	54.12	54.59	85.85	81.32
Oxygen	42.52	41.96	14.15	18.68
Sulfur	1.41	2.11	–	–
Silicon	0.82	–	–	–
Nitrogen	1.13	1.33	–	–

Table 5
At.% of C-containing functional groups and C/O ratio obtained through XPS C1s spectra fitting.

Sample	Csp^2 (%)	Csp^3 (%)	C-O/C-N (%)	C=O (%)	COOH (%)	C/O
GO-1	16.6	24.8	44.1	8.9	5.7	1.70
GO-2	15.4	26	40.1	10.8	7.7	1.73
rGO-1	74.5	2.7	15.5	4.5	2.8	5.80
rGO-2	74.2	5.0	13.8	3.9	3.0	8.09

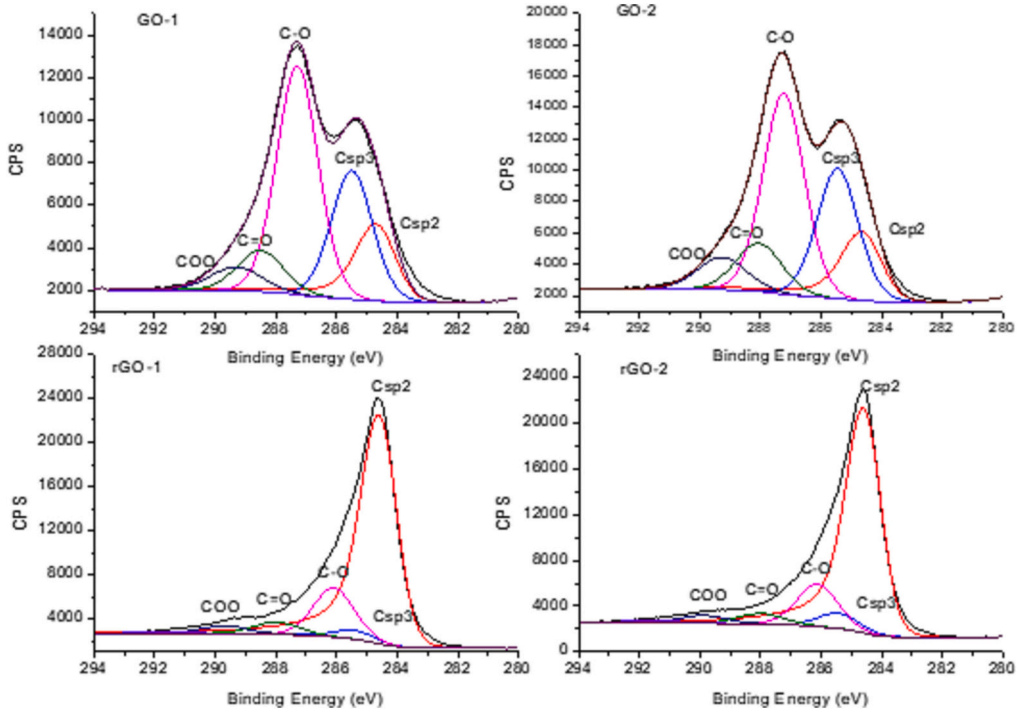

Fig. 10. Curve fitting of the C1s XPS spectra of the GO and rGO samples.

after thermal reduction treatment at 400 °C [42], indicating a high reduction degree.

3.6. Fourier-transform infrared spectroscopy (FTIR)

Representative FTIR spectra of the graphene oxides as well as reduced graphene oxides obtained from recycled graphites are shown in Fig. 11. GO-1 and GO-2 present the characteristic FTIR spectral features of highly hydrophilic graphite oxides, which are similar to those obtained from natural graphite powder [43]. Several absorption bands can be appreciated in the (4000–400) cm^{-1} range. Precisely, spectra of our GO samples exhibit several absorption bands peaked at about 1040 cm^{-1}, 1395 cm^{-1}, 1630 cm^{-1}, and 1735 cm^{-1} that can be attributed to the C—O stretching, C-OH bending, C═C stretching, and C═O stretching, respectively [13,15,17]. This result confirms the presence of the mentioned oxygen functional groups in both GOs. These bands were found to disappear and/or dramatically decrease in spectra measured in the corresponding reduced graphene oxides, which agrees with the removal of oxygen-containing functional groups in GO samples [17]. In addition, both spectra show a broad band at 3430 cm^{-1} due to O—H stretching. All the mentioned FTIR bands are much better defined in the spectra of the GO samples, evidencing the oxidation of the starting graphites to graphene oxides. Besides, the existing C = C peak at 1620 cm^{-1} in the spectra of both rGO samples indicates an effective restoration of the π-conjugated structure of carbon atoms [44]. These results strongly suggest that the reduction of both graphene oxides obtained from recycled graphites was carried out satisfactorily.

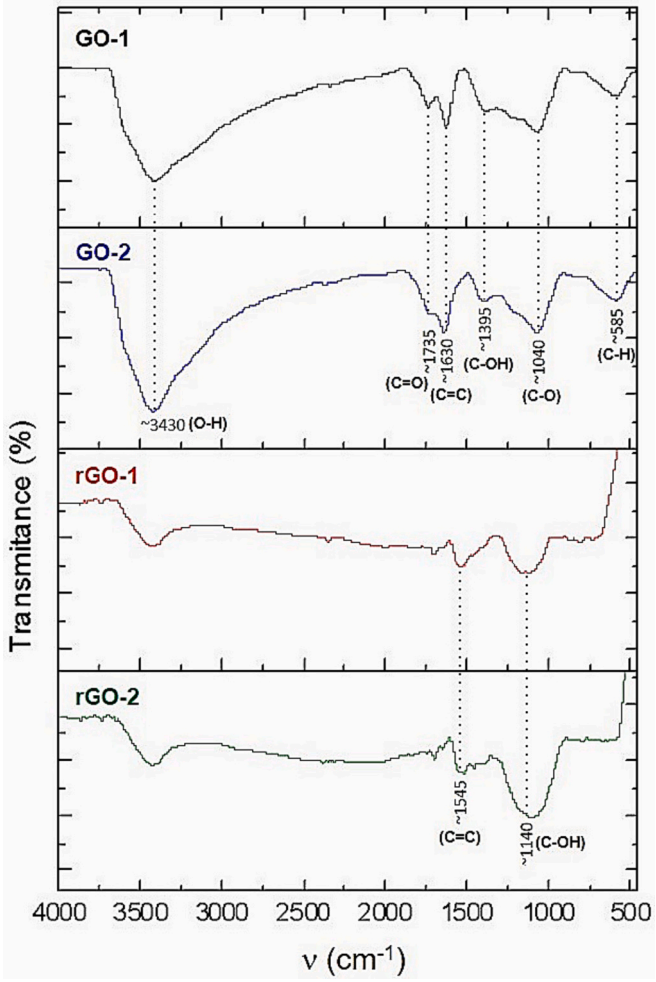

Fig. 11. FTIR spectra of the obtained GOs and rGOs samples.

3.7. Micro-Raman spectroscopy

Raman spectroscopy is a non-destructive technique particularly suitable for the characterization of carbon allotropes and carbon-based materials, providing information regarding its morphology, defect structure, and graphitization degree due to its sensitivity to structural changes [45,46]. XRD provides long-range structural information and is not a spatially-resolved technique – which means that averages the structural characteristics of GO and rGO layers and agglomerates with different sizes, morphologies and defects. On the contrary, micro-Raman spectroscopy is able to provide short-range structural information of individual layers and particles, being both techniques complementary. Raman spectra of the GO and rGO samples under 325 nm (UV) excitation are shown in Fig. 12(a), while spectra recorded from the rGO samples under 633 nm excitation are shown in Fig. 12(b). The strong PL emission measured in the latter samples when excited by the 633 nm laser (see Supplementary Material) precluded the obtaining of good quality spectra. In order to gain insight into the structural characteristics of both kinds of samples, spectra were deconvoluted to a sum of Lorentzian profiles. An example of the results obtained for GO and rGO samples under UV excitation are shown in Fig. 13, while the peak position found for all samples appear listed in Table 6. The dominant bands are peaked, under UV excitation, at about 1402 and 1602 cm^{-1} for GO samples and near 1405 and 1597 cm^{-1} for rGO samples and correspond to the well-known D and G bands. In the case of 633 nm excitation (Fig. 14 and Table 6), the D and G bands appear respectively peaked at 1328 and 1595 cm^{-1}. The significant shift of the D band peak position is explained by the dispersive nature of this Raman band [47]. Moreover, UV Raman spectroscopy is particularly sensitive to the sp^3 carbon sites, while visible Raman spectroscopy (633 nm in the present work) is more sensitive to the sp^2-bonded sites, since visible excitation resonates with the π states. In fact, it has been reported that - for several carbon-based materials - UV Raman spectroscopy is the only method to obtain reliable structural information due to the fact that visible Raman spectra of such materials are masked by interference from luminescence or strong scattering from sp^2-bonded carbon atoms [48]. In addition, it can be observed that the I_D/I_G ratio decreases by increasing the laser excitation energy, in agreement with multi-wavelength Raman studies of different carbon compounds [49].

The D peak is a defect-activated band associated to the breathing modes (A_{1g} symmetry) of six carbon-atom rings K-point phonons. The D´ band, peaked at 1625 cm^{-1} in GO spectra and ~ 1617 cm^{-1} in rGO spectra, is also related to defects, and originates from intra-valley one-phonon double resonance Raman processes involving one longitudinal optical phonon near the Γ point of the Brillouin zone (BZ) and one defect. These modes are not Raman active in first order Raman scattering of perfect samples but become Raman active in defective carbon materials owing to defect-induced double resonance Raman scattering processes involving the electronic π–π* transitions [50]. The G band is a doubly degenerate phonon mode (E_{2g} symmetry) at the BZ center that is due to the bond stretching vibrations of all pairs of sp^2 atoms in both rings and chains of carbon networks [51,52]. The 2D band, near 2770 cm^{-1}, is a second order peak that corresponds to the harmonic of an in-plane transverse optical (TO) mode close to the zone boundary K point [50]. Some other bands related to the second order Raman spectrum were found. These appear centered at about 3000 and 3190 cm^{-1} in both GO and rGO spectra and can be attributed to the D + G combination and to the harmonic 2G, respectively. In addition, several additional bands were found to be necessary to properly fit the experimental Raman data. These bands have been labeled for increasing peak wavenumber as P1 to P6 (Tables 6 and 7) and are mainly associated to defects and/or functional groups present in the GO and rGO samples, as explained in the following. It should be mentioned that observation of these bands depends on the sample considered (GO or rGO) and the excitation conditions (UV vs visible laser excitation). P1, centered ~1170 cm^{-1} is a weak band only observed in rGO samples under 633 nm excitation. The origin

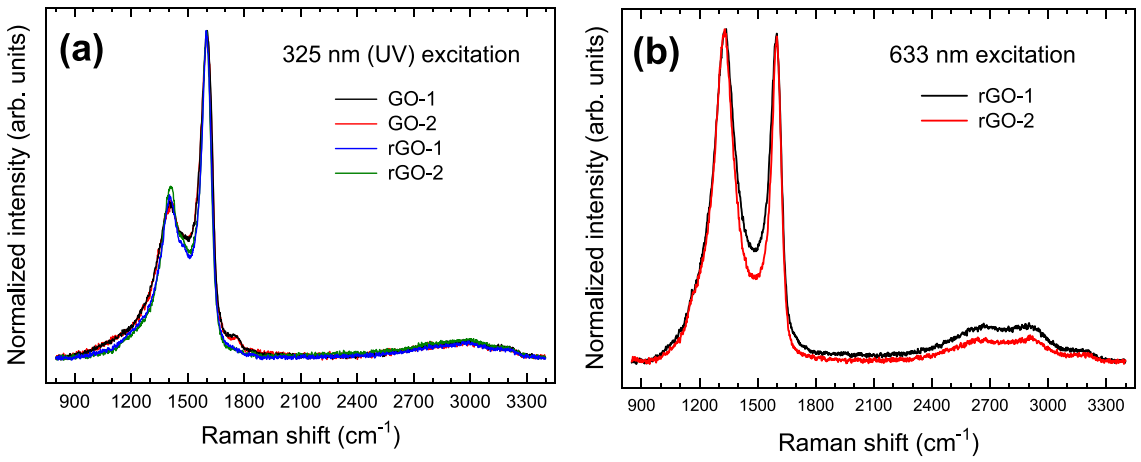

Fig. 12. Normalized Raman spectra of all the GO and rGO samples investigated under UV (325 nm) excitation (a) and Raman spectra of the rGO samples under 633 nm excitation (b).

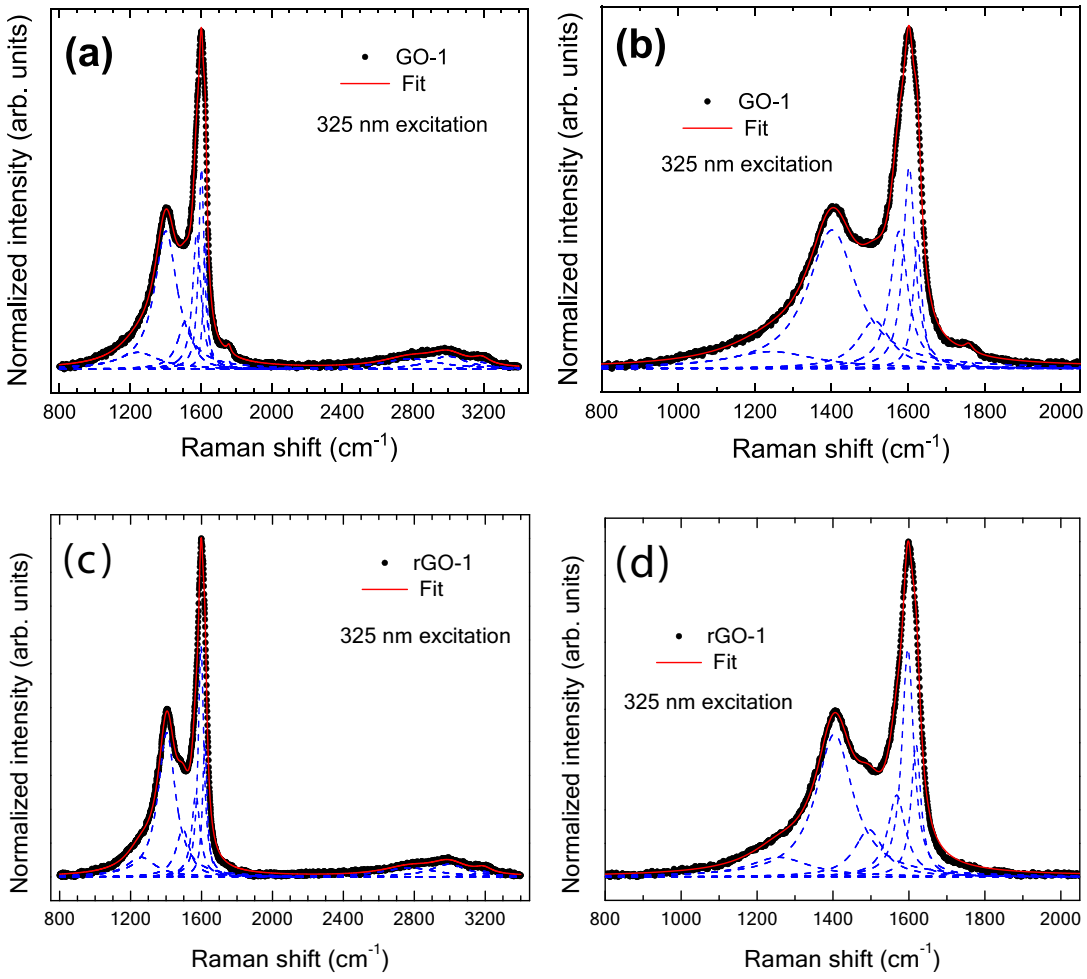

Fig. 13. Lorentzian deconvolution of representative Raman spectra from sample GO-1 and rGO-1 in the (800–3400) cm^{-1} range (a,c) and in the (800–2050) cm^{-1} range (b,d). Circles represent the experimental data while the red solid line corresponds to the best-fit curve. (For interpretation of the references to colour in this figure legend, the reader is referred to the web version of this article.)

of this band, sometimes named D*, is still unclear. It has been observed in many carbon materials, including GO samples with different chemical compositions [53] and nanocrystalline diamond [54]. The mentioned band is usually assigned to sp^3 carbons in amorphous or disordered graphitic lattices [53,54] or to sp^2-sp^3 bonded edge carbon atoms [55], although some authors attribute this peak to C═C stretching and CH wagging modes of *trans*-polyacetylene [54], which is unlikely in our case. Our P2 band is observed centered near 1240–1250 cm^{-1}. A similar band has been observed in Raman spectra of oxidized graphene oxide (OGO) [55] and attributed to COOH/C-OH functional groups, which is

Table 6
Peak position of the bands found by deconvolution of Raman spectra of the investigated samples under UV excitation.

Sample / band	P2	D	P4	P5	G	D´	P6	2D	D + G	2G
GO-1	1243	1402	1512	1577	1603	1625	1759	2787	2998	3190
GO-2	1200	1405	1528	1581	1604	1626	1763	2766	3001	3194
rGO-1	1256	1404	1496	1568	1597	1619	–	2773	2995	3192
rGO-2	1254	1405	1494	1561	1594	1615	–	2771	3001	3192

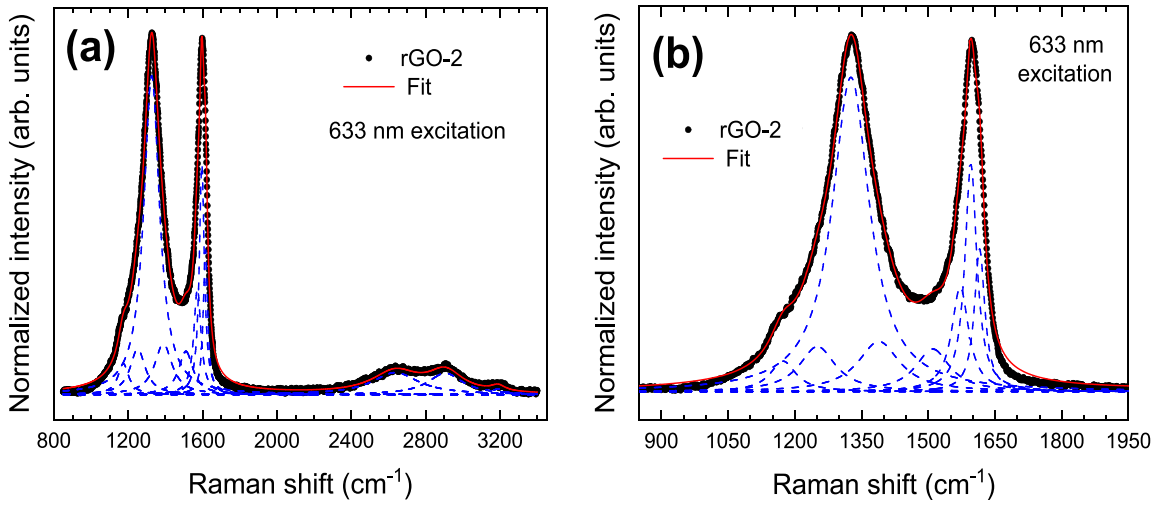

Fig. 14. Lorentzian deconvolution of a representative Raman spectrum from sample rGO-2 in the (800–3400) cm^{-1} range (a) and in the (850–1950) cm^{-1} range. Circles represent the experimental data while the red solid line corresponds to the best-fit curve. (For interpretation of the references to colour in this figure legend, the reader is referred to the web version of this article.)

Table 7
Peak position of the bands found by deconvolution of Raman spectra of the rGO samples under 633 nm excitation.

Sample / band	P1	P2	D	P3	P4	P5	G	D´	2D	D + G	2G
rGO-1	1167	1242	1329	1430	1518	1571	1595	1615	2640	2909	3181
rGO-2	1173	1250	1327	1399	1510	1572	1596	1615	2644	2911	3189

in agreement with our XPS measurements. The peak labeled P3 is observed in the (1400–1430) cm^{-1} range only in rGO material and under visible (633 nm) excitation. Detailed annealing studies carried out in GO have assigned this Raman band, also under 633 nm light excitation, to the covalent attachment of oxygen (C-O/C=O) to edge carbon atoms [55]. As for the P4 peak, the position and behaviour of this Raman band agrees with that named D´ in previous works on GO samples with different chemical compositions. This band, observed centered between 1505 and 1540 cm^{-1}, has been attributed to amorphous phases in GO [53,56]. The peak position of the mentioned band was found to shift towards smaller wavenumbers as the oxygen content was reduced. In our case, the band appears peaked near 1520 cm^{-1} under UV excitation and at about 1495 cm^{-1} in spectra of reduced samples, in agreement with the described trend. P5 appears centered at ~1580 cm^{-1} in GO spectra and between 1560 and 1570 cm^{-1} in rGO. The proximity of this peak to the G band suggests that it could be related to C=C vibrations of atoms in the close proximity of a functionalized C atom, which would slightly distort the pristine carbon network due to functional groups-induced strain [57]. Band labeled P6, peaked near 1760 cm^{-1}, is very weak and only observed in GO samples. A band at 1750 cm^{-1} has been experimentally observed in GO films [58] and also found to disappear on reduction. This band has been assigned to Stone-Wales defects - also termed 5–7–7-5 rings, since they are made of two heptagonal and two pentagonal carbon rings. Such attribution agrees with DFT calculations carried out for graphite oxide and functionalized graphene, which indicate that the mentioned defects give rise to a Raman band at about 1745 cm^{-1} [59].

3.8. Electrical characterization

I-V curves recorded in all the samples investigated are shown in Fig. 15. Values obtained for GO and rGO samples are comparable or even larger than those reported in the literature for samples grown by the Hummers method from commercial graphite flakes [57,59,60] or purified natural graphite [61]. As expected, reduction significantly increases conductivity. Actually, the conductivity of the rGO samples was found to be almost three orders of magnitude larger than that of the starting GO material. Such enhancement agrees with the increased C/O ratio determined from our EDX, XRF and XPS measurements. In fact, rGO often shows a semiconductor behaviour, depending on the corresponding band gap width on the kind and concentration of functional groups. Although the effect of many functional groups on the band gap structure of GO and rGO has not been systematically investigated, an increased concentration of oxygen-containing groups generally increases the band gap width and reduces the electrical conductivity [62]. Transitions from insulating to semiconducting to semi-metallic behaviour have been experimentally observed in GO samples obtained by different methods depending on the reduction degree and physico-chemical characteristics of the starting materials [63,64]. These transitions are generally attributed to an increase of the number and size of sp^2 domains - separated by non-reduced sp^3 areas - as reduction proceeds, which might even lead to the formation of percolated sp^2 networks. This is supported

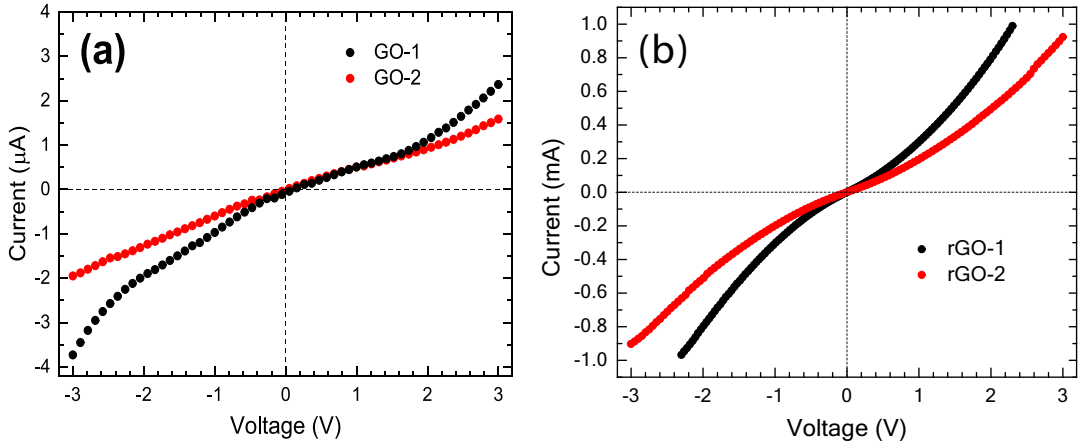

Fig. 15. Representative I-V curves recorded in the investigated GO (a) and rGO samples (b).

by our XPS measurements, showing a clear increase of the Csp^2 / Csp^3 ratio in the investigated rGO samples, as compared with that measured in GO. For moderate reduction, charge transport is thought to be ruled by variable range hopping [59,65], a mechanism involving inelastic tunneling that has been observed in other disordered carbon compounds [66] and that accounts for the non-linear character of the recorded I-*V* curves together with the Schottky type GO/rGO-metal electrode contacts [59].

3.9. Potential applications of the obtained graphene-based materials

In spite of not being flat materials, its wrinkled structure - as well as its abundant surface oxygen-containing functional groups - may be advantageous and allow the obtained GOs to exhibit specific characteristics that could be useful for potential applications [67]. Obtained GOs are ideal to be chemically modified with organic compounds to prepare composites which can be used as coatings with anticorrosive applications [68]. This is useful because these nanocomposites exhibit remarkable gas barrier properties that can be applied to effectively reduce oxygen and water vapor permeability which is a key aspect in the development of electronic devices. Environmental applications of present GOs include its potential for effectively removing toxic gases. According to the literature, layered wrinkled GO structures present selective channels for gas separation with excellent preferential CO_2 permeation performance [69]. Since prepared GOs exhibit high hydrophilicity, they are suitable to prepare graphene oxide membranes with ability for bind heavy metals which is useful in water treatment and analytical applications [70–72].

Potential applications of the obtained rGOs are linked to its high conductivity and its remarkable SSA values. The high surface area and porous structure of rGO improve electron mobility, which is crucial for energy storage applications such as supercapacitors [73]. The obtained SSA for rGO-2 is close to those observed for highly reduced graphene oxide (HRGO) based capacitors (468 $m^2 \cdot g^{-1}$) [74]. Another interesting capability of the synthesized rGOs concerns its use in sorbents with superior performance relative to pure materials. Catalytic applications of rGO-based sorbents include a wide range of processes mainly related with the environment and energy generation fields [75–79]. SSA values of most employed rGOs for such applications range from 50 to 400 $m^2 \cdot g^{-1}$, which encompass the SSA values of rGOs obtained in this work. In a recent study, the suitability of rGO-NiO-ZnO based sorbents for hydrogen sulfide removal from syngas has been demonstrated [80]. Since our rGO-2 presents a SSA value (381 $m^2 \cdot g^{-1}$) very close to that measured for rGO used in the above-mentioned work (403 $m^2 \cdot g^{-1}$), the use of rGO-2 obtained from the black mass recovered from spent batteries represents an interesting and feasible alternative for this kind of technological application.

4. Conclusions

GO and rGO have been synthesized by using graphite extracted by two different acid leaching methods from black masses of spent vehicle LIBs as starting material. As compared with previous works based on the recycling of a single battery from a small-scale device, the precursor material here used is representative of a larger-scale recycling procedure, involves the processing of both cathodic and anodic materials, and concerns a larger number of batteries from different sources (vehicles) and operated in diverse conditions. The morphology, chemical features, structure and electrical properties of the samples have been thoroughly investigated by using several complementary characterization techniques.

The GO samples were obtained by the Marcano-Tour method. No significant differences were observed for both GOs, being very similar to those obtained from natural graphite. Hence, the use of citric acid for the black mass treatment is highly recommended in order to reduce the use of toxic and non-environmentally friendly reagents. SEM images show a distinctive wrinkled morphology which is partially lost due to layer stacking after annealing treatments carried out to obtain the corresponding rGO samples. XRD patterns show the expected maxima for GO and rGO materials and no secondary phases. XRF and SEM-EDX results evidence the existence of small amounts of different impurities in the samples, in particular uniformly distributed silica and alumina microparticles. BET measurements show rGO specific surface areas in the (195–385) m^2/g range, which are comparable to those measured in rGO obtained from non-recycled graphite precursors. The existence of several oxygen-containing functional groups was assessed by FTIR and XPS measurements. The kind and concentration of these groups were not found to depend significantly on the leaching conditions used to obtain the precursor graphites. Thermal annealing leads to a decreased concentration of these groups and the corresponding increment of the C concentration in both rGO materials. Deconvolution of Raman spectra acquired under different excitation conditions reveals bands that can be attributed to different kinds of defects in the carbon network of the samples as well as bands that can be attributed to some of the O-containing functional groups observed by XPS. Electrical measurements show that the conductivity of our GO and rGO samples are very similar or even larger than those reported for samples obtained from commercial graphite or purified natural graphite. Based on the characterization results of the obtained graphene-related materials the potential capabilities of both GOs and rGOs make them a suitable alternative for a great variety of uses in different fields. Our work evidence this is a cost-effective and sustainable route to obtain graphene-based materials with highly competitive properties, contributing to the circular economy and the recyclability of wastes which are traditionally discarded.

CRediT authorship contribution statement

Lorena Alcaraz: Conceptualization, Data curation, Investigation, Methodology, Writing – original draft, Writing – review & editing. **Carlos Díaz-Guerra:** Conceptualization, Data curation, Investigation, Methodology, Resources, Writing – review & editing. **Rodolfo Fernández-Martínez:** Data curation, Investigation, Methodology, Writing – review & editing. **M. Belén Gómez-Mancebo:** Data curation, Methodology, Writing – review & editing. **Belén Sotillo:** Data curation, Investigation, Methodology, Writing – review & editing. **Irene Llorente:** Data curation, Writing – review & editing. **Félix A. López:** Conceptualization, Data curation, Investigation, Methodology, Resources, Writing – review & editing.

Declaration of competing interest

The authors declare that they have no known competing financial interests or personal relationships that could have appeared to influence the work reported in this paper.

Data availability

The data that has been used is confidential.

Acknowledgments

This work was carried out as part of the activities of the CSIC Interdisciplinary Thematic Platform PTI Mobility 2030. The authors gratefully acknowledge the financial support of the European Union, Horizon Europe Programme (HORIZON) through project FREE4LIB Ref. 101069890. This work has been partially supported by Banco Santander-UCM through project PR87/19-22613 and by Comunidad de Madrid through Project PR65/19-22464 (Proyectos de I + D para jóvenes doctores).

Appendix A. Supplementary data

Supplementary data to this article can be found online at https://doi.org/10.1016/j.matchar.2024.113695.

References

[1] B. Niu, J. Xiao, Z. Xu, Advances and challenges in anode graphite recycling from spent lithium-ion batteries, J. Hazard. Mater. 439 (2022) 129678, https://doi.org/10.1016/j.jhazmat.2022.129678.

[2] L.A. Romo, A. López-Fernández, I. García-Díaz, P. Fernández, A. Urbieta, F. A. López, From spent alkaline batteries to Zn x Mn 3−x O 4 by a hydrometallurgical route: synthesis and characterization, RSC Adv. 8 (2018) 33496–33505, https://doi.org/10.1039/C8RA06789A.

[3] L.-P. He, S.-Y. Sun, Y.-Y. Mu, X.-F. Song, J.-G. Yu, Recovery of Lithium, nickel, cobalt, and manganese from spent Lithium-ion batteries using <scp>l</scp> -tartaric acid as a Leachant, ACS Sustain. Chem. Eng. 5 (2017) 714–721, https://doi.org/10.1021/acssuschemeng.6b02056.

[4] R. Saneie, H. Abdollahi, S. Ghassa, D. Azizi, S. Chehreh Chelgani, Recovery of copper and aluminum from spent Lithium-ion batteries by froth flotation: a sustainable approach, J. Sustain. Metall. 8 (2022) 386–397, https://doi.org/10.1007/s40831-022-00493-0.

[5] Y. Gao, C. Wang, J. Zhang, Q. Jing, B. Ma, Y. Chen, W. Zhang, Graphite recycling from the spent Lithium-ion batteries by sulfuric acid curing-leaching combined with high-temperature calcination, ACS Sustain. Chem. Eng. 8 (2020) 9447–9455, https://doi.org/10.1021/acssuschemeng.0c02321.

[6] J. Yang, E. Fan, J. Lin, F. Arshad, X. Zhang, H. Wang, F. Wu, R. Chen, L. Li, Recovery and reuse of anode graphite from spent Lithium-ion batteries via citric acid leaching, ACS Appl. Energy Mater. 4 (2021) 6261–6268, https://doi.org/10.1021/acsaem.1c01029.

[7] I. Rey, C. Vallejo, G. Santiago, M. Iturrondobeitia, E. Lizundia, Environmental impacts of graphite recycling from spent Lithium-ion batteries based on life cycle assessment, ACS Sustain. Chem. Eng. 9 (2021) 14488–14501, https://doi.org/10.1021/acssuschemeng.1c04938.

[8] L. Alcaraz, C. Díaz-Guerra, J. Calbet, M.L. López, F.A. López, Obtaining and characterization of highly crystalline recycled Graphites from different types of spent batteries, Materials (Basel). 15 (2022) 3246, https://doi.org/10.3390/ma15093246.

[9] P. Joshi, R. Yadav, K.K.H. De Silva, M. Hara, H. Shibuya, Y. Motoyama, M. Yoshimura, Dependence of precursor graphite flake size on nitrogen doping in graphene oxide and its effect on OER catalytic activity, ACS Omega 7 (2022) 29287–29296, https://doi.org/10.1021/acsomega.2c03496.

[10] R. Muzyka, S. Drewniak, T. Pustelny, M. Chrubasik, G. Gryglewicz, Characterization of graphite oxide and reduced graphene oxide obtained from different graphite precursors and oxidized by different methods using Raman spectroscopy, Materials (Basel). 11 (2018) 15–17, https://doi.org/10.3390/ma11071050.

[11] Z. Zhen, H. Zhu, Structure and Properties of Graphene, Graphene, Elsevier, in, 2018, pp. 1–12, https://doi.org/10.1016/B978-0-12-812651-6.00001-X.

[12] Y. Sun, M. Sun, D. Xie, Graphene Electronic Devices, Graphene, Elsevier, in, 2018, pp. 103–155.

[13] R.A. Rochman, S. Wahyuningsih, A.H. Ramelan, Q.A. Hanif, Preparation of nitrogen and Sulphur co-doped reduced graphene oxide (rGO-NS) using N and S heteroatom of thiourea, IOP Conf. Ser. Mater. Sci. Eng. 509 (2019) 012119, https://doi.org/10.1088/1757-899X/509/1/012119.

[14] D. Shahdeo, A. Roberts, N. Abbineni, S. Gandhi, Graphene Based Sensors, Compr. Anal. Chem., Elsevier, 2020, pp. 175–199.

[15] I.O. Faniyi, O. Fasakin, B. Olofinjana, A.S. Adekunle, T.V. Oluwasusi, M.A. Eleruja, E.O.B. Ajayi, The comparative analyses of reduced graphene oxide (RGO) prepared via green, mild and chemical approaches, SN Appl. Sci. 1 (2019) 1181, https://doi.org/10.1007/s42452-019-1188-7.

[16] Y. Ma, L. Zhi, Graphene-based transparent conductive films: material systems, Preparation and Applications, Small Methods. 3 (2019) 1800199, https://doi.org/10.1002/smtd.201800199.

[17] B.D. Ossonon, D. Bélanger, Synthesis and characterization of sulfophenyl-functionalized reduced graphene oxide sheets, RSC Adv. 7 (2017) 27224–27234, https://doi.org/10.1039/C6RA28311J.

[18] V.B. Mohan, K. Lau, D. Hui, D. Bhattacharyya, Graphene-based materials and their composites: a review on production, applications and product limitations, Compos. Part B Eng. 142 (2018) 200–220, https://doi.org/10.1016/j.compositesb.2018.01.013.

[19] W. Lv, Z. Li, Y. Deng, Q.-H. Yang, F. Kang, Graphene-based materials for electrochemical energy storage devices: opportunities and challenges, Energy Storage Mater. 2 (2016) 107–138, https://doi.org/10.1016/j.ensm.2015.10.002.

[20] M.B. Burkholder, F.B.A. Rahman, E.H. Chandler, J.R. Regalbuto, B.F. Gupton, J.M. M. Tengco, Metal supported graphene catalysis: a review on the benefits of nanoparticular supported specialty sp2 carbon catalysts on enhancing the activities of multiple chemical transformations, Carbon Trends. 9 (2022) 100196, https://doi.org/10.1016/j.cartre.2022.100196.

[21] I.-W.P. Chen, Y.-S. Chen, N.-J. Kao, C.-W. Wu, Y.-W. Zhang, H.-T. Li, Scalable and high-yield production of exfoliated graphene sheets in water and its application to an all-solid-state supercapacitor, Carbon N. Y. 90 (2015) 16–24, https://doi.org/10.1016/j.carbon.2015.03.067.

[22] V.B. Mbayachi, E. Ndayiragije, T. Sammani, S. Taj, E.R. Mbuta, A. Ullah Khan, Graphene synthesis, characterization and its applications: a review, Results Chem. 3 (2021) 100163, https://doi.org/10.1016/j.rechem.2021.100163.

[23] J. Walker PL, Chemistry and Physics of Carbon 6, Marcel Dekker, Inc., 1970. New York, Country unknown/Code not available, https://www.osti.gov/biblio/4445451.

[24] T.R. Gengenbach, G.H. Major, M.R. Linford, C.D. Easton, Practical guides for x-ray photoelectron spectroscopy (XPS): interpreting the carbon 1s spectrum, J. Vac. Sci. Technol. A Vacuum, Surfaces, Film. 39 (2021), https://doi.org/10.1116/6.0000682.

[25] A.C. Ferrari, J. Robertson, Interpretation of Raman spectra of disordered and amorphous carbon, Phys. Rev. B 61 (2000) 14095–14107, https://doi.org/10.1103/PhysRevB.61.14095.

[26] H. Park, S. Lim, D. Du Nguyen, J.W. Suk, Electrical measurements of thermally reduced graphene oxide powders under pressure, Nanomaterials. 9 (2019) 1387, https://doi.org/10.3390/nano9101387.

[27] H.F. Teoh, Y. Tao, E.S. Tok, G.W. Ho, C.H. Sow, Electrical current mediated interconversion between graphene oxide to reduced grapene oxide, Appl. Phys. Lett. 98 (2011) 173105, https://doi.org/10.1063/1.3580762.

[28] E.M. Aliyev, M.M. Khan, A.M. Nabiyev, R.M. Alosmanov, I.A. Bunyad-zadeh, S. Shishatskiy, V. Filiz, Covalently modified graphene oxide and polymer of intrinsic microporosity (PIM-1) in mixed matrix thin-film composite membranes, Nanoscale Res. Lett. 13 (2018) 359, https://doi.org/10.1186/s11671-018-2771-3.

[29] R. Fernandez-Martinez, M.B. Gomez-Mancebo, L.J. Bonales, C. Maffiotte, A. J. Quejido, I. Rucandio, Study and comparison of different routes to synthesize reduced graphene oxide, J. Nanopart. Res. 74 (2022) 69–82, https://doi.org/10.4028/p-41b175.

[30] R. Ikram, B.M. Jan, W. Ahmad, An overview of industrial scalable production of graphene oxide and analytical approaches for synthesis and characterization, J. Mater. Res. Technol. 9 (2020) 11587–11610, https://doi.org/10.1016/j.jmrt.2020.08.050.

[31] X. Shen, X. Lin, N. Yousefi, J. Jia, J.-K. Kim, Wrinkling in graphene sheets and graphene oxide papers, Carbon N. Y. 66 (2014) 84–92, https://doi.org/10.1016/j.carbon.2013.08.046.

[32] M. Azarang, A. Shuhaimi, R. Yousefi, M. Sookhakian, Effects of graphene oxide concentration on optical properties of ZnO/RGO nanocomposites and their application to photocurrent generation, J. Appl. Phys. 116 (2014) 084307, https://doi.org/10.1063/1.4894141.

[33] G.T.T. Le, J. Manyam, P. Opaprakasit, N. Chanlek, N. Grisdanurak, P. Sreearunothai, Divergent mechanisms for thermal reduction of graphene oxide

and their highly different ion affinities, Diam. Relat. Mater. 89 (2018) 246–256, https://doi.org/10.1016/j.diamond.2018.09.006.
[34] M.T. Tajabadi, M. Sookhakian, E. Zalnezhad, G.H. Yoon, A.M.S. Hamouda, M. Azarang, W.J. Basirun, Y. Alias, Electrodeposition of flower-like platinum on electrophoretically grown nitrogen-doped graphene as a highly sensitive electrochemical non-enzymatic biosensor for hydrogen peroxide detection, Appl. Surf. Sci. 386 (2016) 418–426, https://doi.org/10.1016/j.apsusc.2016.06.045.
[35] A. Alazmi, O. El Tall, S. Rasul, M.N. Hedhili, S.P. Patole, P.M.F.J. Costa, A process to enhance the specific surface area and capacitance of hydrothermally reduced graphene oxide, Nanoscale. 8 (2016) 17782–17787, https://doi.org/10.1039/C6NR04426C.
[36] R.E. Franklin, The structure of graphitic carbons, Acta Crystallogr. 4 (1951) 253–261, https://doi.org/10.1107/S0365110X51000842.
[37] J.M. Sánchez, E. Ruiz, J. Otero, Selective removal of hydrogen sulfide from gaseous streams using a zinc-based sorbent, Ind. Eng. Chem. Res. 44 (2005) 241–249, https://doi.org/10.1021/ie0497902.
[38] A. Kaushal, S.K. Dhawan, V. Singh, Determination of Crystallite Size, Number of Graphene Layers and Defect Density of Graphene Oxide (GO) and Reduced Graphene Oxide (RGO), 2019 030106, https://doi.org/10.1063/1.5112945.
[39] M.B. Gómez-Mancebo, R. Fernández-Martínez, A. Ruiz-Perona, V. Rubio, P. Bastante, F. García-Pérez, F. Borlaf, M. Sánchez, A. Hamada, A. Velasco, Y. K. Ryu, F. Calle, L.J. Bonales, A.J. Quejido, J. Martínez, I. Rucandio, Comparison of thermal and laser-reduced graphene oxide production for energy storage applications, Nanomaterials. 13 (2023) 1391, https://doi.org/10.3390/nano13081391.
[40] R. Al-Gaashani, A. Najjar, Y. Zakaria, S. Mansour, M.A. Atieh, XPS and structural studies of high quality graphene oxide and reduced graphene oxide prepared by different chemical oxidation methods, Ceram. Int. 45 (2019) 14439–14448, https://doi.org/10.1016/j.ceramint.2019.04.165.
[41] N. Díez, A. Śliwak, S. Gryglewicz, B. Grzyb, G. Gryglewicz, Enhanced reduction of graphene oxide by high-pressure hydrothermal treatment, RSC Adv. 5 (2015) 81831–81837, https://doi.org/10.1039/C5RA14461B.
[42] F. Wu, Q. Zeng, Y. Xia, M. Sun, A. Xie, The effects of annealing temperature on the permittivity and electromagnetic attenuation performance of reduced graphene oxide, Appl. Phys. Lett. 112 (2018), https://doi.org/10.1063/1.5028472.
[43] S. Rattana, N. Chaiyakun, N. Witit-anun, P. Nuntawong, S. Chindaudom, C. Oaew, P. Kedkeaw, Limsuwan, Preparation and characterization of graphene oxide nanosheets, Procedia Eng. 32 (2012) 759–764, https://doi.org/10.1016/j.proeng.2012.02.009.
[44] Y. Su, J. Du, D. Sun, C. Liu, H. Cheng, Reduced graphene oxide with a highly restored π-conjugated structure for inkjet printing and its use in all-carbon transistors, Nano Res. 6 (2013) 842–852, https://doi.org/10.1007/s12274-013-0362-2.
[45] Y. Bai, X. Zhao, T. Li, Z. Lv, S. Lv, H. Han, Y. Yin, H. Wang, First-principles investigation in the Raman and infrared spectra of sp3 carbon allotropes, Carbon N. Y. 78 (2014) 70–78, https://doi.org/10.1016/j.carbon.2014.06.050.
[46] L. Bokobza, J.-L. Bruneel, M. Couzi, Raman spectra of carbon-based materials (from graphite to carbon black) and of some silicone composites, C. 1 (2015) 77–94, https://doi.org/10.3390/c1010077.
[47] I. Pócsik, M. Hundhausen, M. Koós, L. Ley, Origin of the D peak in the Raman spectrum of microcrystalline graphite, J. Non-Cryst. Solids 227–230 (1998) 1083–1086, https://doi.org/10.1016/S0022-3093(98)00349-4.
[48] I. Calizo, I. Bejenari, M. Rahman, G. Liu, A.A. Balandin, Ultraviolet Raman microscopy of single and multilayer graphene, J. Appl. Phys. 106 (2009) 043509, https://doi.org/10.1063/1.3197065.
[49] M.J. Matthews, M.A. Pimenta, G. Dresselhaus, M.S. Dresselhaus, M. Endo, Origin of dispersive effects of the Raman D band in carbon materials, Phys. Rev. B 59 (1999) R6585–R6588, https://doi.org/10.1103/PhysRevB.59.R6585.
[50] A.C. Ferrari, D.M. Basko, Raman spectroscopy as a versatile tool for studying the properties of graphene, Nat. Nanotechnol. 8 (2013) 235–246, https://doi.org/10.1038/nnano.2013.46.
[51] A.C. Ferrari, Raman spectroscopy of graphene and graphite: disorder, electron–phonon coupling, doping and nonadiabatic effects, Solid State Commun. 143 (2007) 47–57, https://doi.org/10.1016/j.ssc.2007.03.052.
[52] M.A. Pimenta, G. Dresselhaus, M.S. Dresselhaus, L.G. Cançado, A. Jorio, R. Saito, Studying disorder in graphite-based systems by Raman spectroscopy, Phys. Chem. Chem. Phys. 9 (2007) 1276–1290, https://doi.org/10.1039/B613962K.
[53] D. López-Díaz, M. López Holgado, J.L. García-Fierro, M.M. Velázquez, Evolution of the Raman Spectrum with the chemical composition of graphene oxide, J. Phys. Chem. C 121 (2017) 20489–20497, https://doi.org/10.1021/acs.jpcc.7b06236.
[54] A. Kaniyoor, S. Ramaprabhu, A Raman spectroscopic investigation of graphite oxide derived graphene, AIP Adv. 2 (2012), https://doi.org/10.1063/1.4756995.
[55] G. Rajender, P.K. Giri, Formation mechanism of graphene quantum dots and their edge state conversion probed by photoluminescence and Raman spectroscopy, J. Mater. Chem. C 4 (2016) 10852–10865, https://doi.org/10.1039/C6TC03469A.
[56] S. Claramunt, A. Varea, D. López-Díaz, M.M. Velázquez, A. Cornet, A. Cirera, The importance of Interbands on the interpretation of the Raman Spectrum of graphene oxide, J. Phys. Chem. C 119 (2015) 10123–10129, https://doi.org/10.1021/acs.jpcc.5b01590.
[57] C. Punckt, F. Muckel, S. Wolff, I.A. Aksay, C.A. Chavarin, G. Bacher, W. Mertin, The effect of degree of reduction on the electrical properties of functionalized graphene sheets, Appl. Phys. Lett. 102 (2013) 023114, https://doi.org/10.1063/1.4775582.
[58] K.N. Kudin, B. Ozbas, H.C. Schniepp, R.K. Prud'homme, I.A. Aksay, R. Car, Raman spectra of graphite oxide and functionalized graphene sheets, Nano Lett. 8 (2008) 36–41, https://doi.org/10.1021/nl071822y.
[59] C. Gómez-Navarro, R.T. Weitz, A.M. Bittner, M. Scolari, A. Mews, M. Burghard, K. Kern, Electronic transport properties of individual chemically reduced graphene oxide sheets, Nano Lett. 7 (2007) 3499–3503, https://doi.org/10.1021/nl072090c.
[60] D.-T. Phan, G.-S. Chung, P–n junction characteristics of graphene oxide and reduced graphene oxide on n-type Si(111), J. Phys. Chem. Solids 74 (2013) 1509–1514, https://doi.org/10.1016/j.jpcs.2013.02.007.
[61] I. Jung, D.A. Dikin, R.D. Piner, R.S. Ruoff, Tunable electrical conductivity of individual graphene oxide sheets reduced at "low" temperatures, Nano Lett. 8 (2008) 4283–4287.
[62] Y. Jin, Y. Zheng, S.G. Podkolzin, W. Lee, Band gap of reduced graphene oxide tuned by controlling functional groups, J. Mater. Chem. C 8 (2020) 4885–4894, https://doi.org/10.1039/C9TC07063J.
[63] G. Eda, C. Mattevi, H. Yamaguchi, H. Kim, M. Chhowalla, Insulator to semimetal transition in graphene oxide, J. Phys. Chem. C 113 (2009) 15768–15771, https://doi.org/10.1021/jp9051402.
[64] Y. Wang, L. Wang, H.-Y. Wang, Q.-D. Chen, H.-B. Sun, Ultrafast spectroscopic study of insulator–semiconductor–semimetal transitions in graphene oxide and its reduced derivatives, J. Phys. Chem. C 123 (2019) 22550–22555, https://doi.org/10.1021/acs.jpcc.9b03926.
[65] C. Mattevi, G. Eda, S. Agnoli, S. Miller, K.A. Mkhoyan, O. Celik, D. Mastrogiovanni, G. Granozzi, E. Garfunkel, M. Chhowalla, Evolution of electrical, chemical, and structural properties of transparent and conducting chemically derived graphene thin films, Adv. Funct. Mater. 19 (2009) 2577–2583, https://doi.org/10.1002/adfm.200900166.
[66] J. Robertson, Amorphous carbon, Adv. Phys. 35 (1986) 317–374, https://doi.org/10.1080/00018738600101911.
[67] X. Zeng, B. Zhu, W. Qiu, W. Li, X. Zheng, B. Xu, A review of the preparation and applications of wrinkled graphene oxide, New Carbon Mater. 37 (2022) 290–302, https://doi.org/10.1016/S1872-5805(22)60594-8.
[68] M.-I. Necolau, A.-M. Pandele, Recent advances in graphene oxide-based anticorrosive coatings: an overview, Coatings. 10 (2020) 1149, https://doi.org/10.3390/coatings10121149.
[69] J. Shen, G. Liu, K. Huang, W. Jin, K.-R. Lee, N. Xu, Membranes with Fast and Selective Gas-Transport Channels of Laminar Graphene Oxide for Efficient CO 2 Capture, Angew. Chemie Int. Ed., 2014 https://doi.org/10.1002/anie.201409563.
[70] A. Alsalme, H. Ahmad, R.A. Khan, B.H. Koo, G.M. Alharbi, S.I. Alhadlaq, Preconcentration and solid phase extraction of trace metal ions by chemically modified graphene oxide Nanoconstructs, Water. 15 (2023) 1121, https://doi.org/10.3390/w15061121.
[71] G. Zhao, J. Li, X. Ren, C. Chen, X. Wang, Few-layered graphene oxide Nanosheets as superior sorbents for heavy metal ion pollution management, Environ. Sci. Technol. 45 (2011) 10454–10462, https://doi.org/10.1021/es203439v.
[72] L. Zhu, X. Guo, Y. Chen, Z. Chen, Y. Lan, Y. Hong, W. Lan, Graphene oxide composite membranes for water purification, ACS Appl. Nano Mater. 5 (2022) 3643–3653, https://doi.org/10.1021/acsanm.1c04322.
[73] Q. Ke, J. Wang, Graphene-based materials for supercapacitor electrodes – a review, J. Mater. 2 (2016) 37–54, https://doi.org/10.1016/j.jmat.2016.01.001.
[74] C. Wang, J. Zhou, F. Du, Synthesis of highly reduced graphene oxide for supercapacitor, J. Nanomater. 2016 (2016) 1–7, https://doi.org/10.1155/2016/4840301.
[75] M.I. Fadlalla, S.G. Babu, Role of Graphene in photocatalytic water splitting for hydrogen production, in: Graphene-Based Nanotechnologies Energy Environ., Elsevier, 2019, pp. 81–108, https://doi.org/10.1016/B978-0-12-815811-1.00005-3.
[76] A. Hasani, M.A. Teklagne, H.H. Do, S.H. Hong, Q. Van Le, S.H. Ahn, S.Y. Kim, Graphene-based catalysts for electrochemical carbon dioxide reduction, carbon, Energy. 2 (2020) 158–175, https://doi.org/10.1002/cey2.41.
[77] S. Karimi, A. Tavasoli, Y. Mortazavi, A. Karimi, Enhancement of cobalt catalyst stability in Fischer–Tropsch synthesis using graphene nanosheets as catalyst support, Chem. Eng. Res. Des. 104 (2015) 713–722, https://doi.org/10.1016/j.cherd.2015.10.016.
[78] S. Wang, H. Sun, H.M. Ang, M.O. Tadé, Adsorptive remediation of environmental pollutants using novel graphene-based nanomaterials, Chem. Eng. J. 226 (2013) 336–347, https://doi.org/10.1016/j.cej.2013.04.070.
[79] P. Yaengthip, A. Siyasukh, L. Payattikul, T. Kiatsiriroat, K. Punyawudho, The ORR activity of nitrogen doped-reduced graphene oxide below decomposition temperature cooperated with cobalt prepared by strong electrostatic adsorption technique, J. Electroanal. Chem. 915 (2022) 116366, https://doi.org/10.1016/j.jelechem.2022.116366.
[80] J.M. Sánchez-Hervás, M. Maroño, R. Fernández-Martínez, I. Ortiz, R. Ortiz, M. B. Gómez-Mancebo, Novel ZnO-NiO-graphene-based sorbents for removal of hydrogen sulfide at intermediate temperature, Fuel. 314 (2022) 122724, https://doi.org/10.1016/j.fuel.2021.122724.